1. Report No.

UB-23-RP-02

2. Government Accession No

N/A

3. Recipient’s Catalog No.

N/A

4. Title and Subtitle

3D Printed Advanced Materials to Mitigate Prestressed Concrete Girder End Cracks

5. Report Date

December, 2025

6. Performing Organization Code

N/A

7. Author(s)

Pranay Singh, Mr., https://orcid.org/0000-0001-6169-9482
Ravi Ranade, Dr., http://orcid.org/0000-0001-6030-8371
Chi Zhou, Dr., http://orcid.org/0000-0001-7230-3754
Pinar Okumus, Dr., http://orcid.org/0000-0002-2197-3261

8. Performing Organization Report No.

UB-23-RP-02

9. Performing Organization Name and Address

University at Buffalo, The State University of New York,
212 Ketter Hall, Buffalo, NY 14260-4300

10. Work Unit No.

N/A

11. Contract or Grant No.

69A3552348333

12. Sponsoring Organization Name and Address

Transportation Infrastructure Precast
Innovation Center (TRANS-IPIC)
University of Illinois Urbana-Champaign.
Civil & Environmental Engineering.
205 N Mathews Ave, Urbana, IL 61801

US Department of Transportation
Office of Research, Development and
Technology (RD&T)
1200 New Jersey Avenue, SE
Washington, DC 201590

13. Type of Report and Period Covered
Final Report

September 2023 - December 2025

14. Sponsoring Agency Code

N/A

15. Supplementary Notes

For additional reports and information visit the TRANS-IPIC website https://trans-ipic.illinois.edu

16. Abstract

Pretensioned bridge girders with thin, deep webs often suffer anchorage-zone cracking during prestress release, leading to durability issues such as chloride ingress and strand corrosion. This study proposes a 3D-printed ductile concrete cover at anchorage zones to prevent macro-cracks from occurring at the external surface. A performance-based design approach integrating structural analysis, material development, and fabrication is adopted. Nonlinear finite element analyses defined hardened-state requirements, while experiments established rheological properties for printability. Beam tests confirmed that tensile strain capacity above 0.6%—achievable with strain-hardening cementitious composites—is essential. Interlayer bonding in 3D-printed concrete was improved through optimized printing parameters. Surface imperfections enhanced bonding between 3D-printed and conventional concrete. Durability and structural tests demonstrated improved crack control and performance, offering a practical pathway to integrate 3D-printed ductile concretes into girders while preserving efficiency and economy.

17. Key Words

Prestressed concrete girders; Anchorage zones; Crack control; Durability; Strain-hardening cementitious composites; 3D concrete printing

18. Distribution Statement

No restrictions.

19. Security Classification (of this report)

Unclassified.

20. Security Classification (of this page)

Unclassified.

21. No. of Pages

57

22. Price

N/A

Disclaimer:

Transportation Infrastructure Precast Innovation Center (TRANS-IPIC)

University Transportation Center (UTC)

3D Printed Advanced Materials to Mitigate Prestressed Concrete Girder End Cracks
UB-23-RP-02

FINAL REPORT

Submitted by:
Ravi Ranade, Associate Professor, ranade@buffalo.edu
Department of Civil, Structural and Environmental Engineering
University at Buffalo

Co-PIs: Chi Zhou (chizhou@buffalo.edu) and Pinar Okumus (pinaroku@buffalo.edu), University at Buffalo

Collaborators / Partners:
None

Submitted to:
TRANS-IPIC UTC
University of Illinois Urbana-Champaign
Urbana, IL

Executive Summary:

Pretensioned concrete bridge girders with thin and deep webs are susceptible to anchorage-zone cracking during prestress release due to the transfer of large prestressing forces over short lengths and the limited tensile capacity of conventional concrete. These cracks compromise durability by facilitating moisture and chloride ingress, accelerating corrosion of prestressing strands and reinforcement. This study investigates a materials-based mitigation strategy that replaces localized macro-cracking with distributed micro-cracking by using a 3D-printed ductile concrete cover applied to critical anchorage zones. The proposed approach integrates structural analysis, material design, and fabrication considerations, and demonstrates improved crack control and durability while maintaining compatibility with conventional precast concrete construction practices.

Objectives:

- Evaluate the feasibility of using a ductile concrete cover to mitigate anchorage-zone cracking in pretensioned concrete girders
- Develop a performance-based design framework for a 3D-printable ductile cementitious material
- Establish structural, rheological, and bonding requirements for practical implementation of 3D-printed concrete covers
- Assess the structural and durability performance of reinforced concrete elements incorporating 3D-printed covers

Methodology:

Nonlinear finite element analyses were conducted to determine strain demands and target hardened-state mechanical properties for anchorage zones. A 3D-printable ductile concrete (a strain-hardening cementitious composite) meeting the target mechanical properties and fresh properties for printability was developed through iterative laboratory testing. The interlayer bonding within the 3D-printed material and the interfacial bonding between conventional and ductile concretes were evaluated, and multiple methods to improve these bonds were explored. Finally, the influence of the proposed ductile concrete cover on the durability of cylindrical specimens (under accelerated corrosion) and the structural performance of beams (under flexure and shear) was assessed and compared with that of control specimens.

Key findings and recommendations:

- For the example prestressed concrete girder modeled in this study, anchorage-zone crack mitigation requires a ductile material with a tensile strain capacity exceeding 0.6%, achievable using strain-hardening cementitious composites.
- Printability of the ductile concrete, containing polymer fibers, is governed by a narrow range of rheological properties that must be controlled for successful fabrication.
- Interlayer bonding in 3D-printed concrete is lower than the intrinsic tensile capacity of the material, but can be improved through optimization of printing parameters and nozzle geometry.
- Surface imperfections inherent to 3D printing significantly enhance bonding between the ductile cover and conventional concrete.
- Durability testing and beam experiments demonstrate improved performance of concrete elements incorporating 3D-printed ductile covers.
- The proposed approach offers a viable pathway for integrating advanced cementitious materials into bridge girders to improve crack control and durability without replacing conventional concrete systems.
- Future implementation should focus on optimizing interfacial bonding, scaling fabrication methods for precast production, and validating performance under field conditions.

Table of Contents

1. Problem description 6
2. Background 7
3. Research scope and objectives 11
    Research Scope 11
    Research Objectives 11
4. Research description 12
5. Project results 37
6. Conclusions and recommendations 51
7. Practical application/impact on transportation infrastructure 52
8. References 54
9. Acknowledgements 57

1. Problem description

Precast, pretensioned concrete bridge girders are a critical component of modern highway infrastructure due to their structural efficiency, rapid construction, and cost-effectiveness. However, these girders are particularly vulnerable to cracking at their ends during prestress release, as shown in Figure 1 [1]. The transfer of large prestressing forces from the steel strands to the surrounding concrete occurs over a relatively short length near the girder ends, resulting in high localized tensile strains. When combined with the inherently brittle nature and low tensile strain capacity of conventional concrete, these concentrated stresses frequently lead to anchorage-zone cracking.

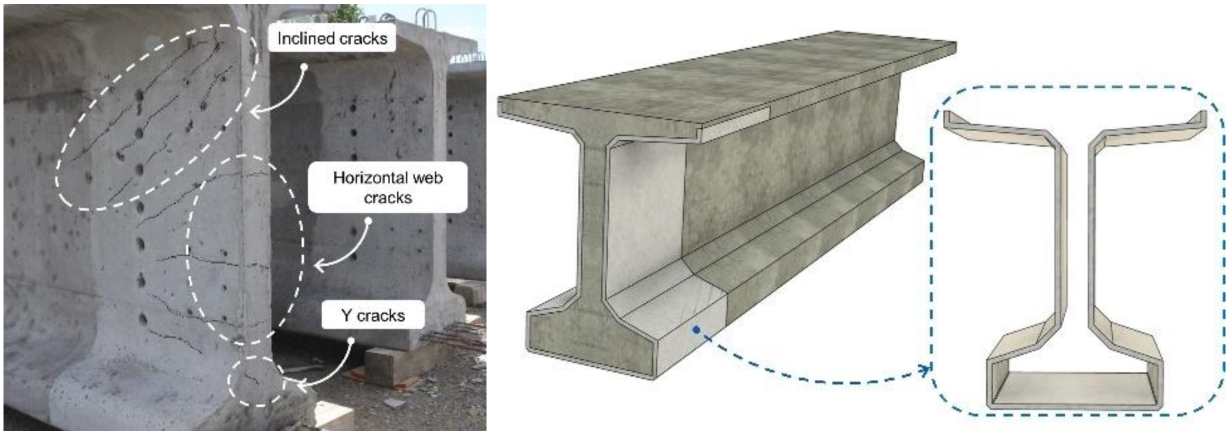

(a) (b)

Figure 1. (a) Typical cracks in the end zone of a pretensioned bulb tee girder [1] (b) 3D-printed SHCC covers as permanent formwork at girder ends

Anchorage-zone cracks represent a significant concern for bridge owners and transportation agencies. Cracks that form near the bottom of the girder are especially problematic, as they may not fully close under service-level live loads [1-3]. Once formed, these cracks provide preferential pathways for moisture and chloride ingress, accelerating corrosion of prestressing strands and reinforcing steel. Over time, such deterioration can compromise the durability, serviceability, and load-carrying capacity of bridge girders, leading to increased maintenance demands, reduced service life, and higher life-cycle costs. Consequently, controlling anchorage-zone cracking remains a persistent challenge in the design and construction of precast-prestressed concrete bridge systems.

To address the limitations of existing crack-control strategies while leveraging the advantages of both advanced materials and additive manufacturing, this study proposes a novel approach: the use of 3D-printed strain-hardening cementitious composite (SHCC) covers at prestressed girder ends. In this concept, the SHCC cover functions as a permanent formwork and a surface crack-control layer, strategically placed in the anchorage zone to accommodate high tensile strains and transform localized macrocracking into distributed microcracking. This approach limits the use of advanced materials to regions where they are most effective, while allowing the bulk of the girder to be constructed using conventional concrete.

2. Background

Several strategies to mitigate cracking at prestressed girder ends have been investigated in the literature. These strategies generally fall into two categories: (i) design and handling-based approaches [4-8], and (ii) materials-based approaches strategies [9, 10]. Design-based strategies typically involve modifications to reinforcement detailing in the anchorage zone, selective debonding of prestressing strands near girder ends, and careful sequencing of strand cutting during prestress transfer. Additional measures include lowering, removing, or spreading out draped strands to reduce tensile strain concentrations at the girder ends. While these methods can reduce cracking severity, they often increase design complexity, require strict construction control, and may not fully eliminate cracking, particularly for girders with increasingly thin and deep webs demanded by modern bridge design.

Materials-based strategies, in contrast, seek to address anchorage-zone cracking by enhancing the tensile response of the concrete itself. Advanced cementitious materials such as ultra-high performance concrete (UHPC) [11] and strain-hardening cementitious composites (SHCC) [12], have demonstrated significantly higher tensile strength and tensile strain capacity compared to conventional concrete. These materials can redistribute stresses by forming multiple fine microcracks rather than localized macrocracks, thereby improving crack control and durability. Previous studies have shown that incorporating such materials at girder ends can effectively reduce anchorage-zone cracking and improve long-term durability [9, 10].

Despite their promising performance, the use of advanced cementitious materials throughout an entire bridge girder is often impractical. Full-section application of UHPC or SHCC introduces challenges related to higher material costs, limited availability, non-standard design provisions, and insufficient long-term data on time-dependent behaviors such as creep, shrinkage, and relaxation in prestressed applications. These constraints limit widespread adoption of advanced materials for full-girder construction in typical bridge projects. An intermediate solution is to limit the use of advanced concrete materials to critical regions, such as girder ends.

Although conceptually attractive, local use of advanced cementitious materials presents several implementation challenges. Conventional casting of localized regions with advanced materials can be labor-intensive, require complex formwork, and raise concerns regarding constructability, interfacial bonding, and quality control. Moreover, ensuring reliable stress transfer between conventional concrete and advanced materials remains a key technical challenge, particularly under repeated loading and environmental exposure. In parallel with advancements in material science, additive manufacturing technologies such as 3D concrete printing have emerged as transformative tools for construction. These technologies offer flexibility in geometry, controlled material placement, and the potential for reducing labor and formwork requirements. However, their application in structural bridge components remains limited, particularly in hybrid systems that combine printed and cast materials.

2.1 Strain-hardening cementitious composites

Strain-hardening cementitious composites (SHCC) are a class of fiber-reinforced concretes [12] with very high tensile ductility (greater than 1% in direct tension) and crack control ability compared to conventional concrete. The crack widths in SHCC are often limited to below 100 µm, which facilitates excellent durability [13, 14]. Fine crack widths significantly reduce permeability and slow the ingress of chlorides, moisture, and other aggressive agents. These properties make SHCC particularly attractive for durability-critical regions of concrete structures, such as bridge decks, joints, and anchorage zones.

Despite their favorable performance, widespread adoption of SHCC and similar advanced materials in prestressed concrete girders has been limited. The primary barriers include higher material costs, lack of standardized design provisions, and uncertainties associated with long-term time-dependent behavior, such as creep, shrinkage, and relaxation, particularly in prestressed applications. Additionally, replacing an entire girder with advanced materials may be unnecessary and inefficient, given that critical tensile demands are typically localized near the girder ends.

As a result, a performance-targeted material development and deployment philosophy has gained increasing attention [15, 16]. Under this framework, advanced materials are strategically placed only in regions where their enhanced properties are required, while the remainder of the structure is constructed using conventional materials. For prestressed girders, the anchorage zone represents a region for such localized intervention, as it experiences the highest tensile strain demand and governs durability performance.

2.2 3D-printing of Strain-Hardening Cementitious Composites

Extrusion-based 3D concrete printing has emerged as a promising construction technology that enables the fabrication of complex geometries without traditional formwork. However, adapting SHCC for 3D printing poses significant technical challenges due to its fiber content and rheological sensitivity [17-21]. Successful printing of SHCC requires careful control of fresh-state properties to ensure continuous extrusion, stable filament formation, and adequate buildability. Fiber dispersion must be maintained throughout mixing, pumping, and extrusion to prevent clogging or nonuniform mechanical behavior. At the same time, the material must retain sufficient tensile ductility after printing to preserve its strain-hardening characteristics.

Recent studies have demonstrated that SHCC can be successfully adapted for extrusion-based printing through optimized mixture design and control of printing parameters [21, 22]. These studies have shown that printed SHCC retains tensile strain-hardening behavior comparable to that of mold-cast specimens. However, the layer-by-layer nature of printing introduces inherent anisotropy, with interlayer interfaces often acting as planes of weakness [23, 24]. Addressing interlayer bonding is therefore critical for structural applications, particularly those involving tensile and flexural loading. Despite these challenges, the ability to precisely place SHCC where needed, combined with its superior crack control characteristics, makes 3D-printed SHCC a compelling candidate for localized durability enhancement in prestressed concrete structures.

2.3 3D-printed Permanent Formworks

Unlike conventional formwork, which is removed after casting, permanent formwork remains as an integral part of the structural system and may contribute to load transfer, durability, or both [25-28]. In prestressed concrete girders, 3D-printed SHCC shells can serve as permanent formwork at the girder ends, providing a ductile outer layer that protects the underlying concrete from cracking and environmental exposure. Such shells can be designed with tailored thickness, geometry, and surface features to enhance bonding with the cast concrete core. Printing-induced surface roughness or intentional geometric interlocking can further improve composite action between the shell and the core.

Previous research has explored printed permanent formworks for beams, columns, and facade elements, demonstrating feasibility and structural compatibility under various loading conditions [25-28]. However, application of this concept to prestressed bridge girders, particularly for addressing anchorage-zone cracking, remains largely unexplored. The integration of performance-targeted SHCC materials with 3D-printed permanent formwork represents a novel strategy to enhance durability while maintaining the efficiency of conventional prestressed concrete construction.

2.4 Integration of 3D-printed covers at precast girder end zones

This study explores the use of a 3D-printed SHCC shell as permanent formwork at the girder's end zone to mitigate cracking. This method leverages the tensile ductility and crack-control capability of SHCC while using conventional concrete as the primary structural component. Figure 2 shows a representative diagram of the proposed SHCC shell surrounding a girder end, and Figure 3 shows a potential workflow for integrating additive manufacturing of the shell with conventional fabrication of a precast bridge girder.

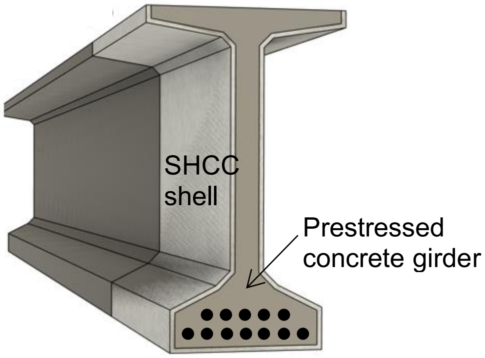

Figure 2. Incorporating SHCC shell at a prestressed concrete girder end

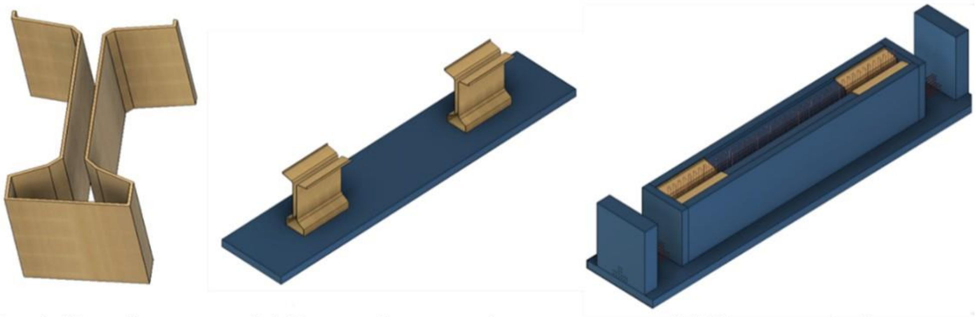

(a) 3D-printing of covers (b) Cover placement on prestressing bed (c) Placement of strands, rebar and molds

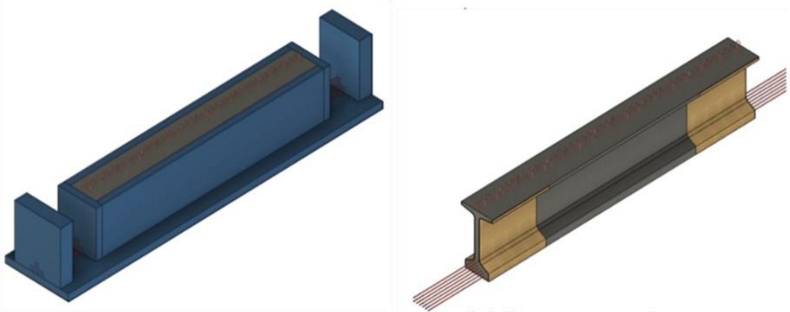

(d) Concrete pouring (e) Prestress release and demolding

Figure 3. Tentative workflow for integration of 3D printed covers at precast girder end as permanent formwork

The integration method consists of two broad stages. The first stage includes printing of the SHCC cover shell. This stage can be performed either at the precast facility or at any other location with a 3D printer. Once the printed covers are cured, they can then be transported to the precaster's facility. In the second stage, these printed covers can be incorporated into the usual precast workflow with minimal changes. The only change required would be to place these covers appropriately on the prestressing bed to allow them to act as permanent formwork within the removable steel formwork for the precast girders. This stage is shown in Figure 3(b). Once these covers are placed, the prestressing strands and rebar cage can be installed as shown in Figure 3(c). The rebar and the cage will not hinder these 3D-printed covers, as the covers have an opening at the top. Subsequently, concrete can be poured as shown in Figure 3(d). Later, the prestressing strands can be released and the molds removed. At this stage, the prestressed bridge girder will have a cover to prevent any undesirable cracking on its surface. The cover is intended to prevent the ingress of any deleterious materials that could affect the service life of the bridge girders.

2.5 Performance-based material design framework for covers

The present study aims to develop a 3D-printable SHCC for the shell application. The performance requirements of the SHCC shell are translated into fresh and hardened material properties through a combination of numerical analysis and experimentation. Starting with a non-printable SHCC with tensile strain capacity greater than 1%, modifications were made to the material ingredients and their proportions to achieve the target properties, as discussed in the following sections of the report.

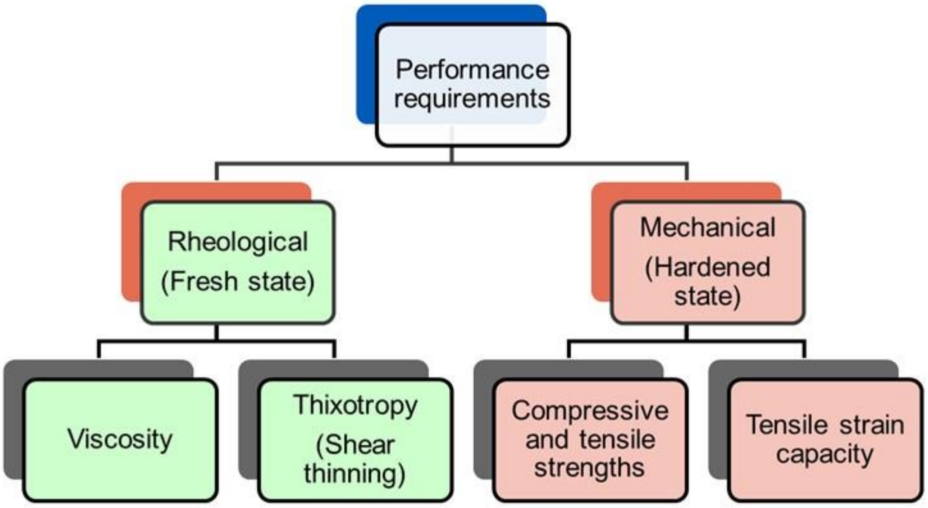

Figure 4. Framework used for designing printable SHCC

3. Research scope and objectives

Research Scope

This research aims to develop a novel crack-mitigation strategy for precast-prestressed concrete bridge girders by using 3D-printed strain-hardening cementitious composite (SHCC) cover shells in critical anchorage zones. The study integrates structural analysis, materials engineering, and additive manufacturing to address anchorage-zone cracking through localized deployment of ductile cementitious materials. The work is limited to laboratory-scale investigations and does not include full-scale girder fabrication or field deployment. The outcomes are intended to inform future implementation and technology transfer efforts.

Research Objectives

Objective 1: Investigate the feasibility of using SHCC shells for mitigating end cracking in precast-prestressed concrete beams

The feasibility was assessed by examining whether SHCC shells met critical performance requirements for anchorage zone, including tensile strain capacity, 3D printability, crack width control, interfacial bonding with conventional concrete, and durability under cracked conditions. The evaluation was conducted through numerical analysis, material characterization, and small-scale beam testing to determine the ability of a 3D-printable SHCC to provide adequate strength, strain compatibility, and crack mitigation for the girder end application.

Objective 2: Develop a 3D-printable SHCC and appropriate printing parameters for the proposed application

An SHCC mixture that satisfies both hardened-state mechanical performance requirements and fresh-state rheological requirements for 3D printing was developed. Material design was guided by performance-based targets derived from numerical modelling. Printing parameters, including extrusion rate, layer height, printing speed, and nozzle geometry, were systematically optimized to achieve stable filament deposition, dimensional accuracy, and buildability for shell geometries relevant to girder ends.

Objective 3: Evaluate the composite action between SHCC shells and conventional concrete

The composite action achieved between the 3D-printed strain-hardening cementitious composite (SHCC) shell and the conventionally cast concrete substrate was evaluated. Load transfer mechanisms across the interface were examined through mechanical testing of reinforced concrete beam specimens in the critical flexural cracking zone. The results of this investigation provided proof of concept and informed the development and planning of subsequent objectives in this study.

Objective 4: Characterize and modify the bond between printed SHCC and conventionally cast concrete under various loading conditions

The interfacial bond behavior between printed strain-hardening cementitious composite (SHCC) and conventional concrete in both axial and shear directions was evaluated. Experimental studies were conducted to determine bond strength and were compared with performance limits established through numerical investigations. Based on these findings, bond enhancement strategies, including printing-induced surface roughness and sandblasting, were explored to improve interfacial performance and ensure reliable stress transfer under prestress loading conditions representative of the example girder.

Objective 5: Evaluate and improve the bond between filament layers of SHCC

The interlayer bond strength was characterized through mechanical testing to assess its influence on tensile behavior in the weak orthogonal direction of printing. The study explored the effects of printing parameters, including layer height, extrusion rate, and nozzle design, on interlayer bonding.

Objective 6: Investigate the durability of cracked concrete specimens protected by printed SHCC cover-shells

The effectiveness of SHCC shells in enhancing the durability of concrete elements by limiting surface crack widths and reducing chloride-ion ingress was evaluated. Durability performance of specimens protected by SHCC shells was compared with that of unprotected control specimens.

Objective 7: Implement the SHCC cover shell concept in laboratory-scale beam specimens

The structural viability of the proposed concept was tested through laboratory-scale reinforced-concrete beam specimens incorporating SHCC shells in critical cracking regions. The impact of the shells on load-carrying capacity, stiffness, crack development, and failure modes under flexural and shear loading was evaluated. These tests validated the concept at the structural level and identified any unintended effects on global behavior.

Objective 8: Optimize 3D printer parameters for constructing SHCC cover-shells

The printer hardware (built in-house) and process parameters were adjusted to ensure consistent and reproducible construction of SHCC shells. Parameters such as extrusion rate, nozzle geometry, layer height, and printing speed were optimized to improve print quality, dimensional stability, interlayer bonding, and surface roughness.

4. Research description

Year 1

An SHCC developed in the PI’s laboratory [29] for past projects (not related to 3D printing) served as the starting point for Year 1’s research. This allowed the investigators to begin objectives 1 and 2 simultaneously. The existing (base) SHCC material properties were used to model pretensioned girders, aiming to mitigate cracks at girder ends using a ductile material shell. At the same time, using the existing SHCC mix design as a basis, the material ingredients and their proportions were altered to achieve a printable mixture while preserving the mechanical properties. Ultimately, the level of composite action between SHCC and conventional concrete was tested (objective 3). The specific research tasks for the Year 1 research (numbered 1.X below) are given below:

Task 1.1 Numerical simulation of pretensioned beams with SHCC shells at the end zone

The first part of the study involved developing and calibrating a finite element model (FEM) for anchorage-zone cracking in an example girder. The model was developed using the finite element analysis (FEA) software ABAQUS-2023 [30]. The model's calibration was based on an experimental study by O'Callaghan and Bayrak [31], which includes recorded reinforcement strain data for a pretensioned concrete bridge girder after prestress release. Girder cross-section, prestressing stresses, and anchorage zone reinforcement details were based on the experimental work of O'Callaghan and Bayrak [31], which was used to compare and calibrate the FEM model against reported experimental findings. Based on the experimental study, the Tx46 girder was selected for the FEM simulation.

The element type and size in the numerical simulation were calibrated to match the transverse reinforcement strains observed by O'Callaghan and Bayrak [31] at the end zone of the concrete girder. Based on this calibration, a 50 mm element size was selected for numerical modeling. Subsequently, a 0.75" SHCC cover at the end zones was applied in the numerical model, keeping all other parameters constant. A representative finite element model and observed surface strain profile of the simulated girder end with SHCC cover are shown in Figure 5.

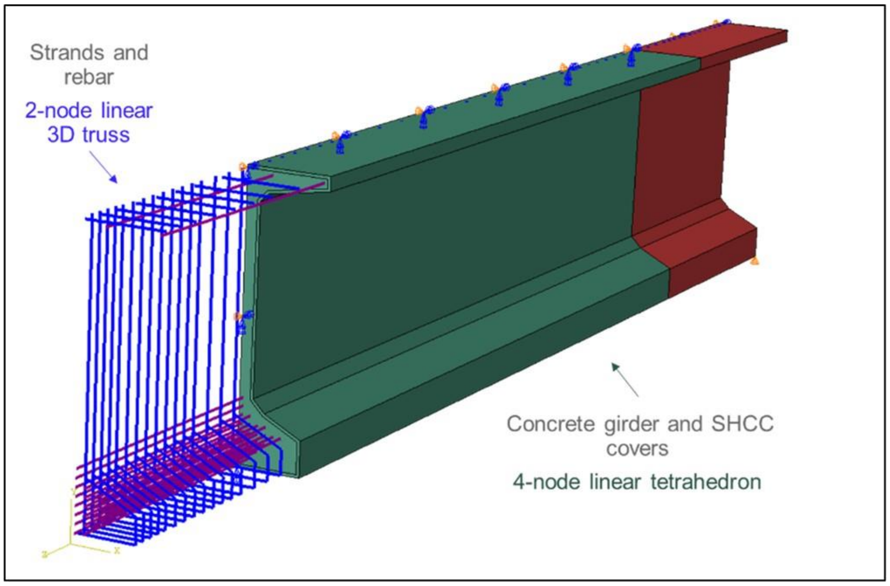

Figure 5. Representative fine element model

Appropriate material models for conventional concrete, SHCC, strands, and rebars were selected. Conventional concrete was modeled using the concrete damage plasticity model in ABAQUS; SHCC was modeled using a trilinear model; and rebar and strands were modeled using bilinear models. Two-node linear 3D truss elements were adopted for strands and rebars. The concrete girder and SHCC cover were modeled using 4-node linear tetrahedron elements. Rebar and prestressing strands were embedded in the girder. The prestressing force was simulated by applying temperature-strain to the strands. The interface between the SHCC cover and the concrete girder was modeled with tie constraints.

Task 1.2 Determination of target material properties for a printable SHCC

The performance requirements for SHCC were categorized into two groups: (i) fresh state requirements and (ii) hardened state requirements. The hardened state properties were determined based on the results of Task 1.1. The fresh state requirements were established for the following five steps of material production and printing:

i. Mixing: Mixing capacity, defined as the maximum shear rate the concrete mixer can apply, was considered to determine the target matrix viscosity required for homogeneous fiber dispersion.
ii. Pumping (Pump): The rheological properties of the SHCC mixture were tuned, and appropriate pumping equipment (motor) was selected to enable continuous pumping while preventing fiber clumping and segregation.
iii. Pumping (Pipe): The rheological properties of the SHCC mixture were also adjusted, and an appropriate pipe diameter and type were selected to prevent blockage and segregation in the pipe.
iv. Extrusion (Nozzle): Blockage at the nozzle and filament tear were minimized by controlling the material's rheological properties and using a customized nozzle (printed separately by the investigators).
v. Layering: Shape retention was achieved by considering the setting characteristics and flow-reduction rates of SHCC mixtures.

It was observed that the above steps required contrasting rheological characteristics, as shown in Figure 6. For example, although a highly viscous mix was suitable for fiber dispersion, segregation prevention, and filament tearing prevention, it caused issues in mixing and pumping due to the available equipment's capacity limitations. High viscosity also increased the risk of blockage during pumping and extrusion.

A flow table test (ASTM C1437) [32] based on relative rheological characterization was implemented in this task due to its simplicity and strong correlations with the material's yield stress and viscosity. The flow table test was used to determine two parameters: (i) Flowability factor and (ii) Flow reduction rate. Flowability factor [33] is defined as the ratio of the diameter of the fresh material sample after 25 drops of the flow table test [34] to the base diameter of the flow cone (100 mm). The flow reduction rate measures the reduction in fresh material's flowability (or thixotropy) over time. Both of these rheological properties are essential for assessing the printability of the material. Suitable ranges for these two parameters were identified to tailor SHCC mixtures.

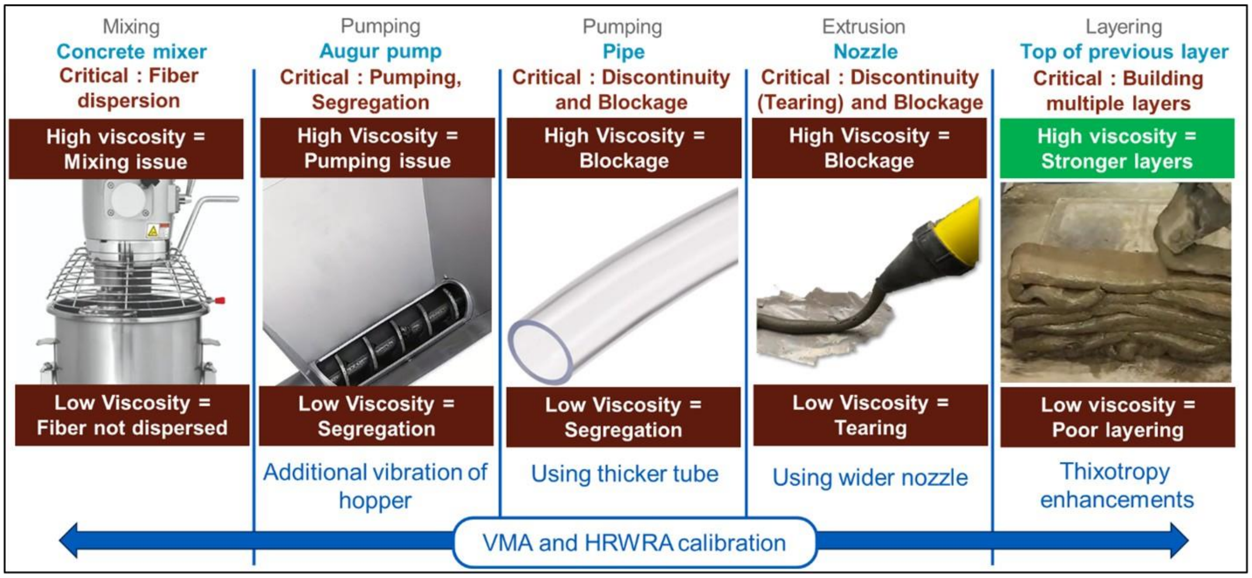

Figure 6. Rheological requirements in various stages, from mixing to printing of SHCC

Task 1.3 Trial mix designs

As mentioned above, an SHCC mixture with high tensile strain capacity but lacking printability, developed previously in PI's lab, was adopted as the baseline. Iterative modifications to the mix were performed as follows to make it 3D-printable:

i. Reduction in water/cementitious material (w/cm) weight ratio: The flow of the baseline SHCC mix was too high for 3D printing. Therefore, as the first step, the w/cm ratio was reduced from 0.38 (in the baseline mixture) to 0.31 to reduce the flow and enhance the compressive strength.

ii. Use of 8 mm PVA fibers: The length of polyvinyl alcohol (PVA) fibers was reduced from 12 mm (in the baseline mixture) to 8 mm to enhance the pumping and extrusion of the mixture.

iii. Adjusting dosages of chemical admixtures: The quantities of High Range Water Reducing Admixture (HRWRA) and Viscosity Modifying Admixture (VMA) were adjusted to achieve the target fresh state characteristics identified in task 2.1. Sixteen mixtures with varying combinations of VMA and HRWRA amounts were prepared and screened using the flowability factors and flow reduction rates. Out of these 16 combinations, four mixtures were found suitable for further optimization.

iv. Enhancement of thixotropic behavior: The mixtures selected in the previous step were further optimized to increase their flow reduction rate. Ingredients such as microsilica, ground silica, and type III cement were incorporated into the mix, and the fresh-state behavior was investigated. Based on the trials performed, three mixtures were selected for further evaluation. The details of these mixtures and the mix design procedure are shown in Figure 7 and in the conference paper referenced below. The outcome was three SHCC mixtures suitable for 3D printing applications.

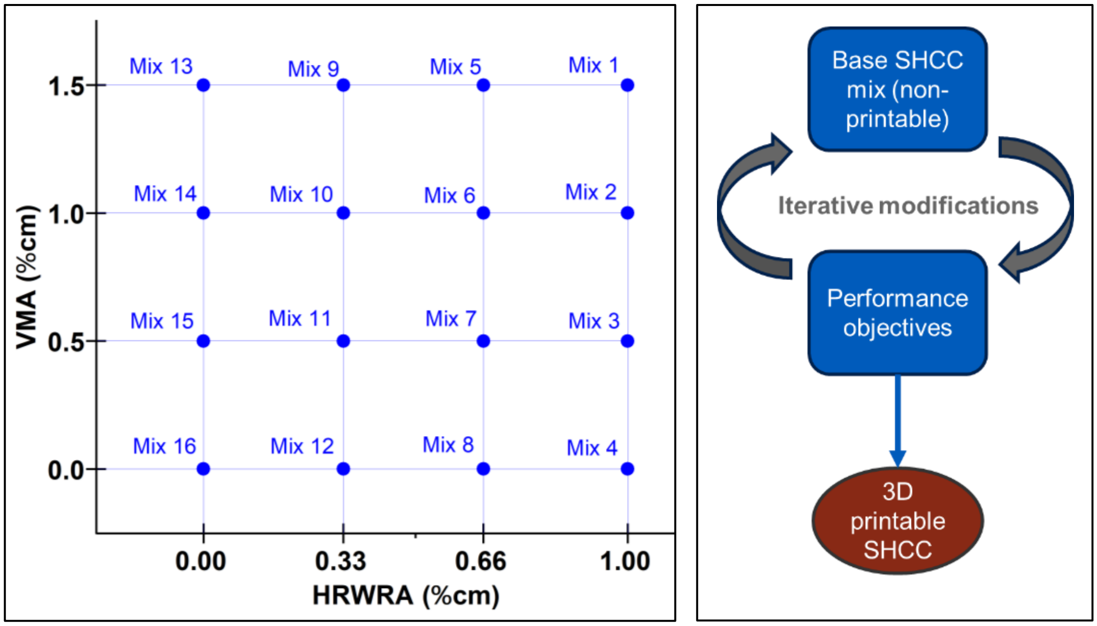

Figure 7. (a) Trial mixtures for rheology optimization of SHCC (b) Iterative mix design procedure

Task 1.4 Testing of fresh and hardened properties and selecting viable mix designs

Fresh-state screening was performed using a caulking gun and a flow table test to reject non-printable mixtures. This screening was performed using qualitative and quantitative criteria, as shown in Figure 8 and described below:

i. Fiber dispersion was checked by hand to assess fiber clumping. The mixtures with observable fiber clumps were rejected.

ii. A grout caulking gun with a nozzle diameter of approximately 0.76″ was used to assess extrudability. Mixes that failed to extrude from this caulking gun were rejected.

iii. Buildability/shape retention: Multiple layers of material were built using a caulking gun. If the base layer of a mix failed to support the weight of at least one other layer, it was rejected.

iv. For relative quantification of the rheological behavior of the developed mix, a flow table test was conducted immediately after mixing and again 30 minutes later to assess flow reduction over time.

v. After each flow table test, the mixtures were observed for segregation/water bleeding, and the mixtures with observable segregation/water bleeding were rejected.

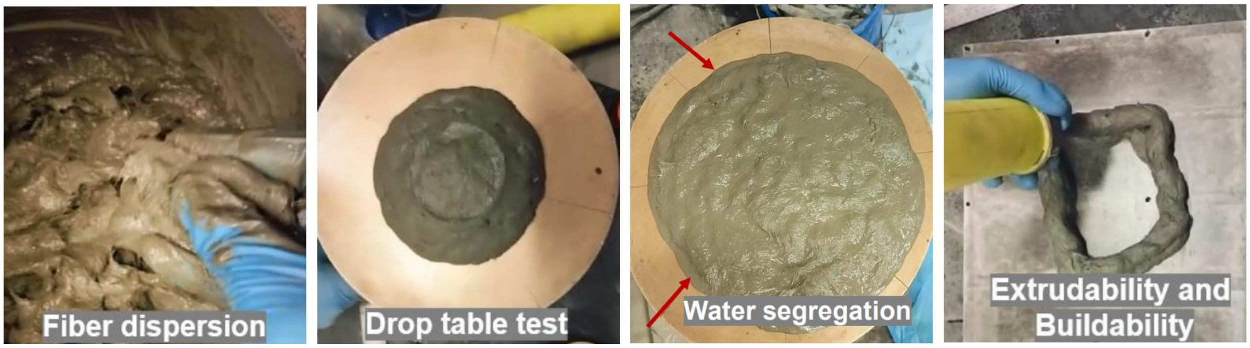

Figure 8. Mix screening protocol based on fresh properties

Hardened properties tests were performed on the screened mixtures. These tests included compressive strength (ASTM C109 [35]), direct tension (ASTM C36 [36]), and four-point flexure tests (ASTM C78 [37]). After initial screening and optimization, three mixtures were selected for further evaluation.

Task 1.5 Mixture refinement

The three printable SHCC mixtures (M9-MS, M9-IS, and M10) were further modified to investigate the effect of the fly ash/cement weight ratio on printability and strain-hardening behavior. Six new mixture compositions (2 variations per mixture) were developed, and their hardened properties, including compressive (per ASTM C109 [35]) and direct tensile [36] behaviors, were evaluated.

Task 1.6 Testing of beams under mechanical loading (Proof of concept stage)

Composite beam specimens were prepared to evaluate the effectiveness of 3D-printed SHCC covers used as permanent formwork for mitigating surface cracking in conventional concrete beams. The experimental program included the design of a suitable conventional concrete mixture, selection of an appropriate beam cross-section, fabrication of 3D-printed SHCC shells, and casting of composite beam specimens.

Conventional concrete mix design: For our planned experimentation, a conventional concrete mix design was adopted from O’Callaghan and Bayrak [31]. Adjustments were made to account for the available raw materials, and the resulting mix design is given in Table 1. The aggregate and cement properties are given in Table 2, and the moisture contents of aggregates are presented in Table 3.

Table 1. Conventional concrete mixture proportions

Material	lb/cyd
Coarse aggregate (SSD)	1709
Fine Aggregate (SSD)	1343
Cement (Type III)	700
Water	245
High Range Water Reducing Admixture, HRWRA	12 oz/Cwt

Table 2. Material properties of conventional concrete’s ingredients

Fine aggregates:	
Fineness modulus	3.74
Bulk specific gravity in SSD state	2.40
Coarse aggregates:	
Nominal maximum aggregate size	0.5”
Bulk specific gravity in SSD state	2.60
Cement:	Type III

Table 3. Moisture content of aggregates used in conventional concrete

	Moisture content (%)	
	Natural	SSD
Coarse aggregates	0.56	0.74
Fine aggregates	4.40	2.40

Cross-section design: Given the project's scope, a trial section for a rectangular beam was designed. The objectives for the design were to achieve a beam section with reasonable rebar sizes and a small (considering 3D printer size, testing equipment capabilities, and minimizing material waste) but sufficient cross-sectional area to accommodate a 3D-printed SHCC shell and a conventional concrete layer in the cover zone. Additionally, the beam was designed to fail in flexure as the SHCC cover is intended for use in the flexural cracking zone.

With these underlying design objectives, multiple cross-sections were explored, and the selected section is shown in Figure 9. The section had a U-shaped 3D-printed SHCC shell with a thickness of 0.8″. A clear spacing of 0.7″ between the 3D-printed cover and stirrups was provided to reduce any hindrance to aggregate flow around the stirrup. Two No. 4 rebars were used as main reinforcement. Additionally, No. 3 rebars with 3″ center-to-center spacing in shear-critical zones and 6″ center-to-center spacing in non-critical zones were employed as stirrups to maintain shear load capacity more than twice the flexural load capacity of the beam.

3D-printing of SHCC cover: An SHCC cover was printed using the M9-MS 3D-printable SHCC mixture developed earlier. As a first step, the printer parameters for the adopted material were optimized to achieve suitable printing. Initial iterations were performed to print a multi-layered wall using the selected mixture, adjusting feed rates and offset distances. The objective was to avoid under-extrusion or scraping (over-extrusion) while printing, as shown in Figure 10. Once finely printed layers were achieved, the cover was printed.

Our laboratory’s existing continuous extrusion system creates material buildup at the ends while printing a U-shape. This problem is not observed with commercial printers. For this research, a rectangular SHCC cover with 5 sides was initially 3D-printed, and 2 sides were cut off to create a U-shaped cover. Two beam specimens were prepared with the above dimensions, as shown in Figure 11. One of the two specimens was a monolithic control specimen made of only conventional concrete, and the other was a composite specimen made with a pre-printed SHCC shell (placed in the middle third of the beam) and conventional concrete. The beams were tested using a four-point bend setup, as shown in Figure 12.

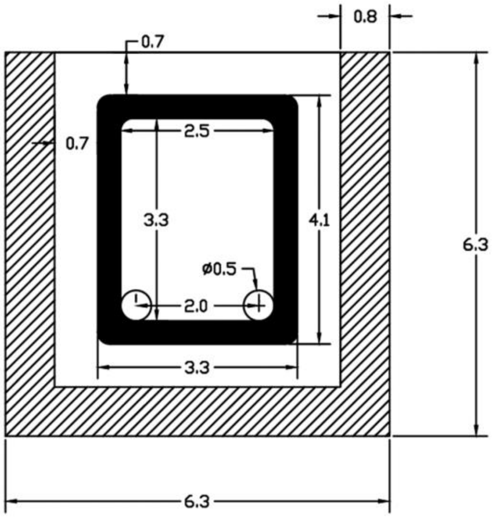

Figure 9. Beam cross-section
(all dimensions in inches rounded to the first decimal place)

Figure 10. Machine-material interaction parameters optimization:
(a) Under-extrusion (b) Over-extrusion (Scraping) (c) Printing with optimized parameters.

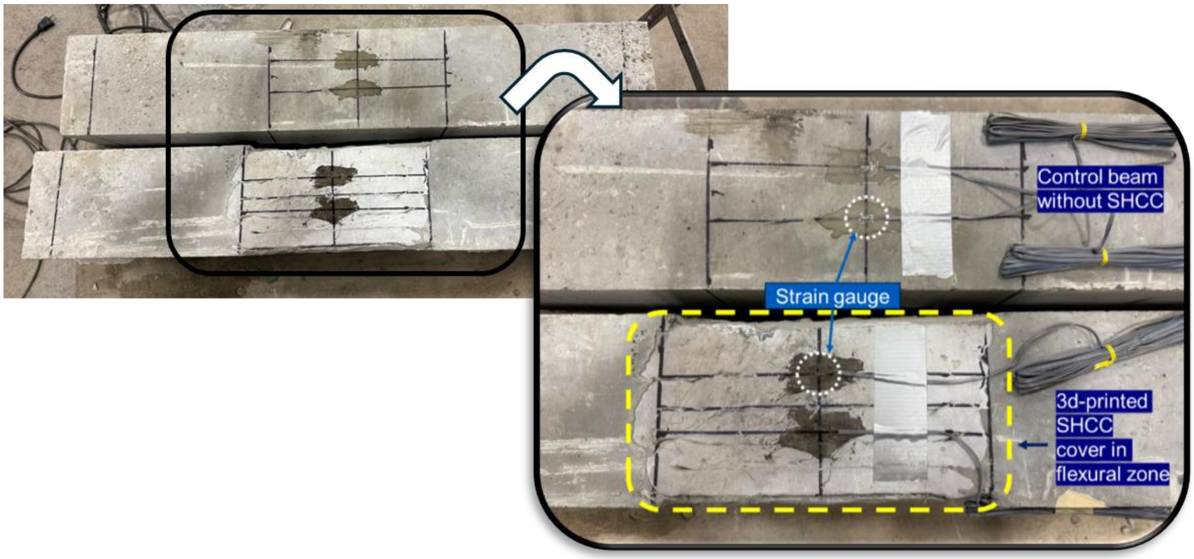

Figure 11. Beam specimens (bottom surface)

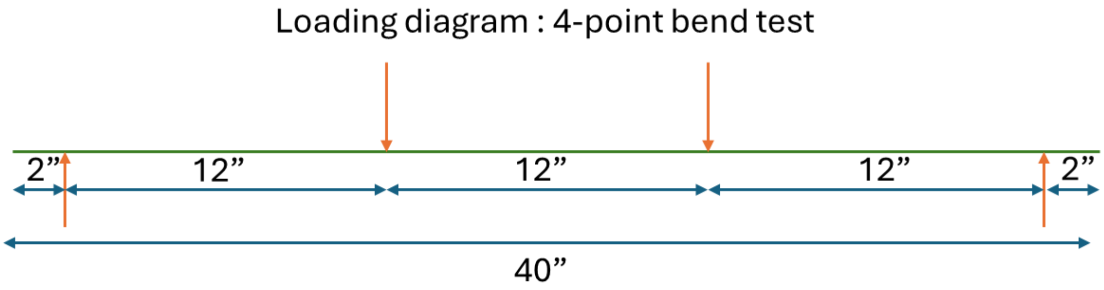

Figure 12. Beam loading diagram

Year 2

Building on the Year 1 research, the Year 2 research tasks focused on the inter-material bond (between concrete and SHCC) and the interlayer bond (between printed SHCC layers), both of which are critical to ensuring the desired performance of the 3D-printed SHCC shell. At the same time, the effect of the 3D-printed SHCC shell on the durability of reinforced-concrete specimens was evaluated. Finally, the constructability of composite beams with 3D-printed SHCC shells was demonstrated. Thus, Year 2 tasks (numbered 2.X below) focused on achieving research objectives 4 to 8 and are described below.

Task 2.1 Inter-material bond characterization

The bond strength between the developed 3D-printable SHCC and a conventional concrete typically used for bridge girders was evaluated through experimental testing. Two complementary experimental methods were employed to characterize the inter-material bonding behavior under axial tension and shear loading.

Axial pull-off experiments were conducted on cylindrical specimens with a bonded circular interface of 3 in. diameter, as shown in Figure 13(a). These specimens were loaded under uniaxial tension to determine the lower bound of the bond strength between SHCC and conventional concrete.

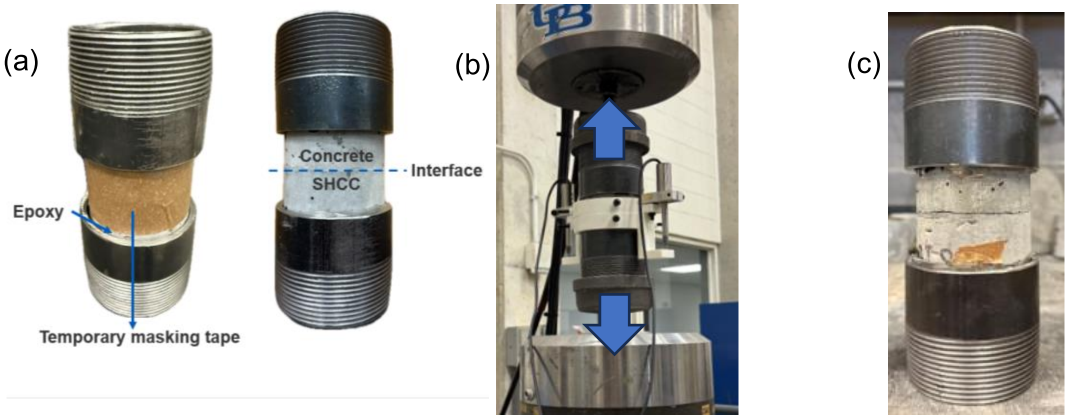

Figure 13. Axial pull-off test (a) Specimen (b) Loading arrangement (c) Interface failure

Shear bond behavior was evaluated using S-shaped specimens with a bonded interface area of 4″x4″, as illustrated in Figure 14. The specimens were loaded in compression to generate a predominantly shear stress state at the bonded interface. This test configuration enabled direct assessment of shear stress transfer across the concrete-SHCC interface.

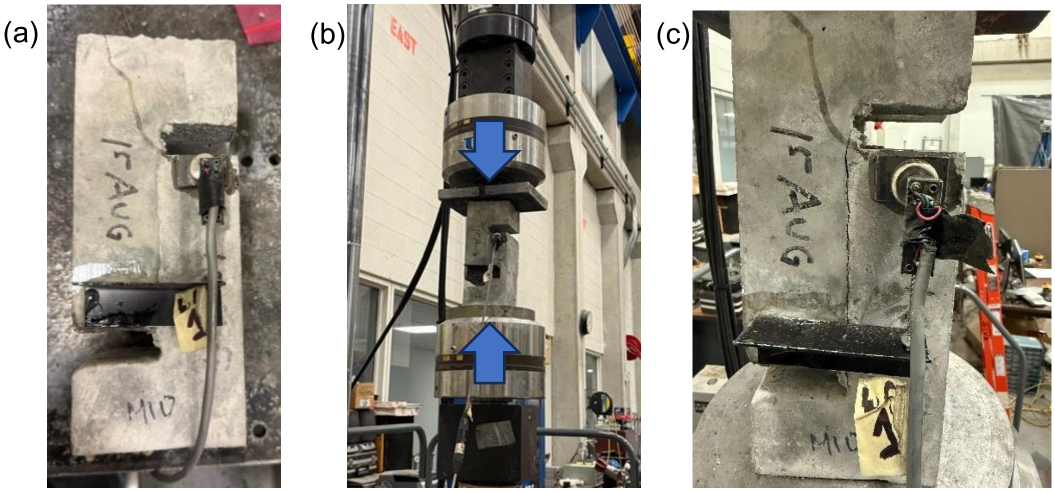

Figure 14. Shear test (a) Specimen (b) Loading arrangement (c) Interface failure

Task 2.2 Numerical modeling of interlayer bonding

For the numerical model developed in Year 1, the concrete–SHCC interface was idealized as perfectly bonded, implying full strain compatibility and no relative slip or separation between the two materials. This assumption was adopted to establish conservative bond-strength demands to ensure composite action between the concrete and the SHCC cover under representative loading conditions.

In Year 2, the numerical model was modified to simulate stress transfer across the concrete–SHCC interface under axial tension and shear loading. Interface stresses were extracted from numerical results to quantify the bond strength required to maintain composite behavior. This modeling framework enabled the identification of critical bond requirements without introducing additional uncertainty associated with interface slip or degradation mechanisms.

Task 2.3 Mechanical testing of reinforced concrete cylinders

Mechanical testing of cylindrical specimens was conducted to evaluate the influence of 3D-printed SHCC cover-shells on cracking behavior. Two types of cylindrical specimens were prepared: (i) monolithic reinforced concrete cylinders without any surface protection, and (ii) composite cylindrical specimens incorporating 3D-printed SHCC covers and conventional concrete in the core.

All the cylinders were designed with identical overall geometry (6” diameter and 12” height), reinforcement, and concrete mix proportions, to ensure that differences in behavior could be attributed solely to the presence of the SHCC cover. A single #4 rebar was provided at the center of each specimen and pulled in tension to induce cracking in the concrete. The central rebars in both cylinder types were loaded to 20 kips using a servo-hydraulic universal testing machine operated in displacement control at a loading rate of 2 mm/min.

For casting the composite specimens, pre-printed SHCC cover shells, cured for 7 days in water, were used as permanent formwork. Following printing, the reinforcement was placed, and conventional concrete was cast within the SHCC shells. All specimens were cured in water under controlled laboratory conditions for 7 days before testing. The cover thickness was 0.8”. Figures 16 and 17 show the preparation steps for the specimens. The loading arrangement is shown in Figure 18.

Control group

3D printed cylindrical formwork

Figure 16. Conventional and 3D-printed cylinder molds

Figure 17. Preparation of reinforced concrete cylinders with 3D printed SHCC covers

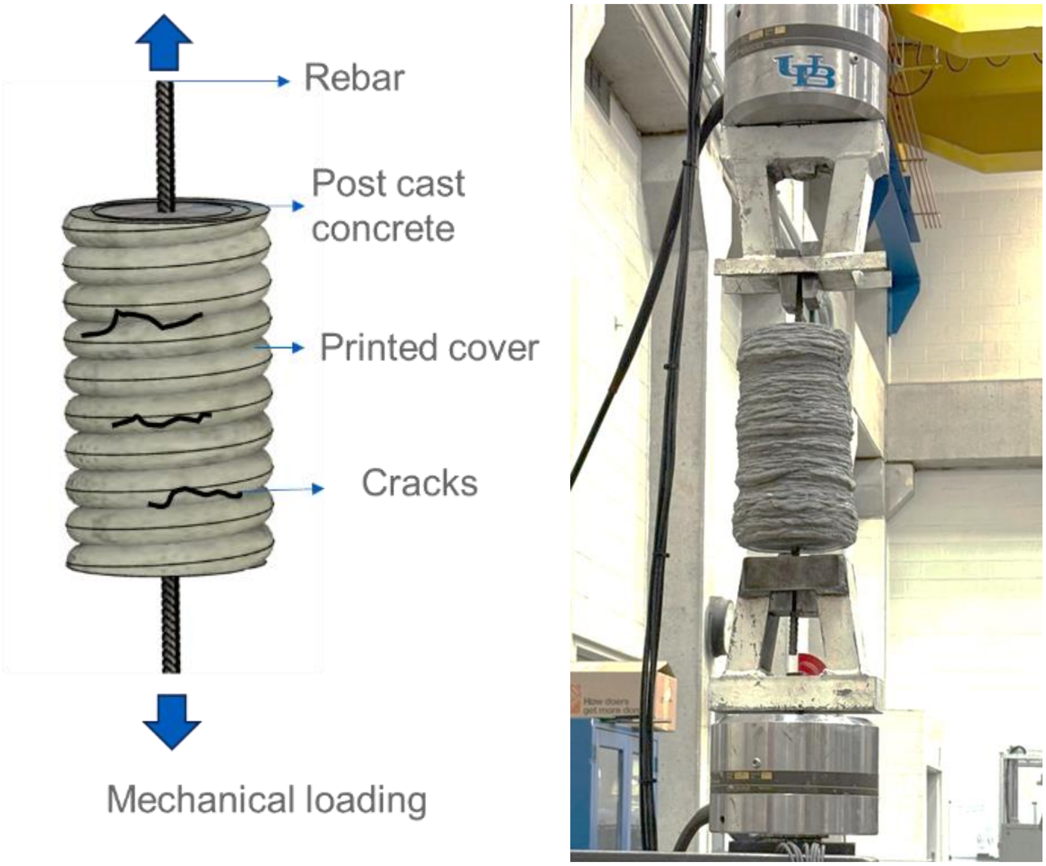

Figure 18. Mechanical loading of cylinders with 3D printed covers

Task 2.4 Bond modifications

The adequacy of the bond strength between conventional concrete and SHCC was evaluated based on the experimental findings obtained from axial and shear bond testing. The results were compared with bond-strength requirements established through numerical analysis to determine whether bond modification was necessary and to assess the effectiveness of proposed improvement strategies.

Bond strength in axial tension

Axial pull-off tests indicated that the concrete–SHCC interface achieved a bond strength of 0.19 ksi. This value exceeded the target axial bond strength of 0.07 ksi, as determined from finite element analysis. The results demonstrated that the bond between SHCC and conventional concrete was sufficient to transfer axial tensile stresses without premature debonding. Consequently, no bond modification was deemed necessary for axial tension.

Bond strength in shear

Shear bond performance was evaluated by comparing experimentally measured bond strength with the shear bond demand obtained from numerical analysis. The required shear bond strength was identified as 0.61 ksi, while experimental shear testing yielded a bond strength of 0.28 ksi. This value was significantly lower than the required shear capacity, indicating that the concrete–SHCC interface was inadequate to resist shear stresses and that bond modification was necessary to enhance shear transfer across the interface.

Bond improvement in shear

Two surface modification techniques were investigated to improve shear bond performance as described below.

Grooved interface

Specimens with grooved interfaces were used to enhance the shear bond between SHCC and concrete. The grooves were introduced through the natural filament layering inherent to the 3D printing process. These grooves were expected to increase shear resistance by promoting mechanical interlocking between the SHCC cover and the conventional concrete substrate.

Sandblasted and grooved interface

To further enhance the shear bond strength, an additional set of specimens was prepared using a combination of grooved interfaces and sandblasting. Sandblasting was applied to expose embedded fibers at the interface, thereby enabling potential fiber bridging and increased frictional resistance under shear loading. The combined use of surface roughening via grooving and fiber exposure via sandblasting was expected to provide synergistic improvement in shear bond strength. Figure 19 shows the surface profiles of the specimens prepared with the two types of bond improvements.

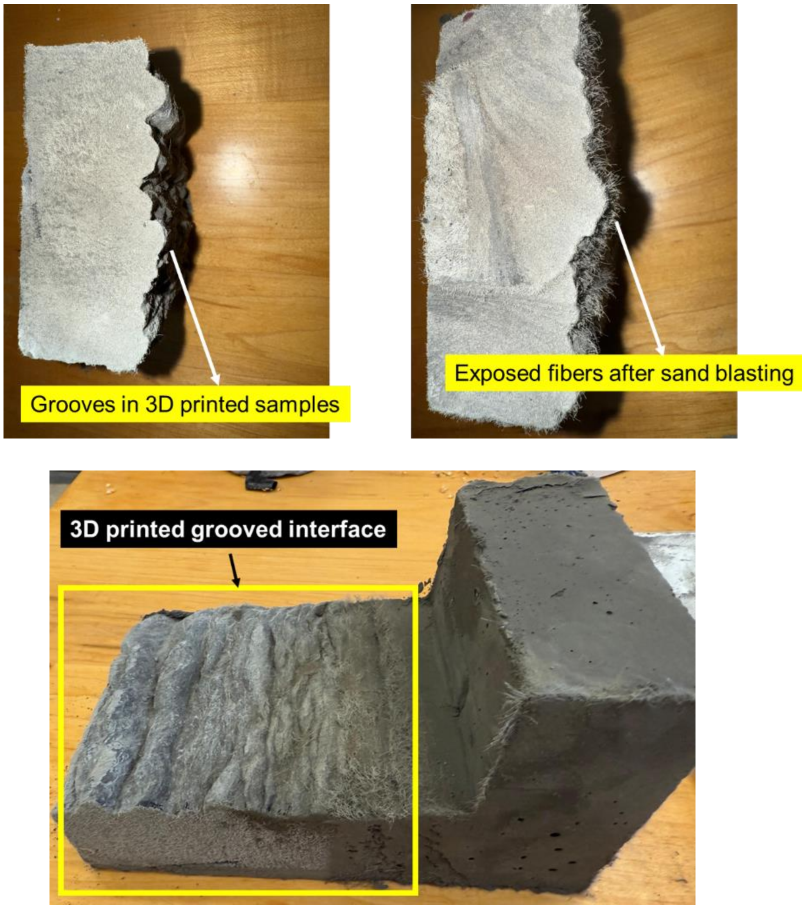

Figure 19. Specimens for bond improvement in shear

Task 2.5 Interlayer bond evaluation

The interlayer bond strength of the 3D-printable SHCC was evaluated using two complementary experimental methods. These tests were designed to quantify tensile resistance across printed layer interfaces and to capture the effects of printing-induced anisotropy on bond performance.

Uniaxial tensile test

Uniaxial tensile tests were conducted to evaluate interlayer bond strength under direct tension. Single-filament–thick SHCC sheets were printed and subsequently cut into dogbone-shaped specimens. The orientation of the specimens was selected such that tensile loading acted across the interlayer interface. The specimens were tested following a protocol similar to that used for tensile characterization of SHCC materials reported in the literature [36]. The tests provided direct measurements of interlayer tensile capacity and enabled comparison with reference axial tensile strengths obtained from cast and printed SHCC specimens.

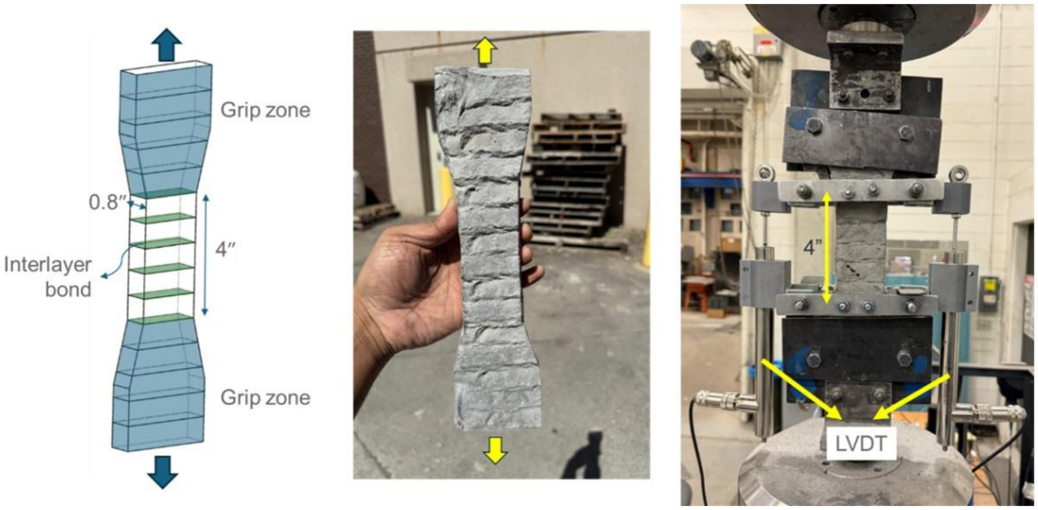

Figure 20. Axial tensile test for interlayer bond strength of 3D printed SHCC

Split tensile test

In addition to direct tension testing, split tensile tests were performed to evaluate interlayer bond strength under indirect tensile loading. Two-layered SHCC sheets were printed and cut into cubic specimens with a total thickness corresponding to two filaments. The specimens were loaded in a compression testing machine using steel cylindrical loading elements positioned at the interlayer interface to induce tensile stresses across the printed layers. Figure 21 shows the test setup and specimen failure pattern for the split tensile test. This testing configuration enabled assessment of interlayer bond behavior under stress states representative of confinement and splitting conditions commonly encountered in structural applications.

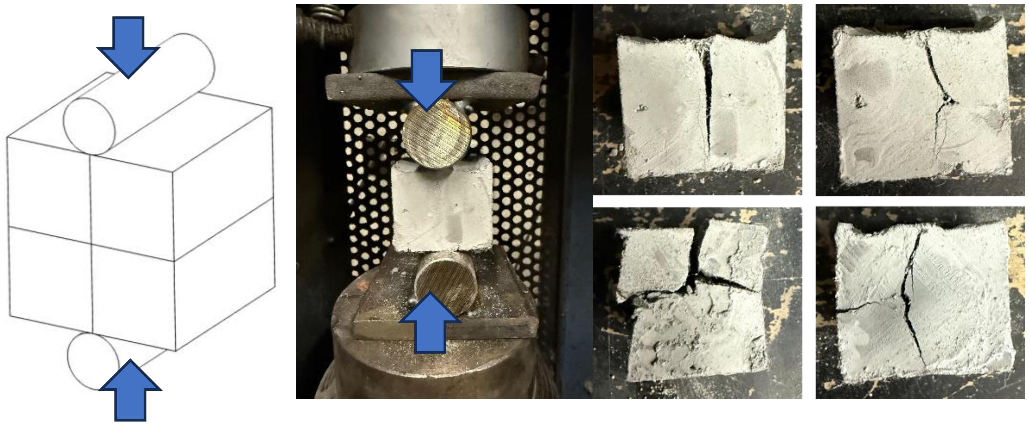

Figure 21. Split tensile test for interlayer bond strength of 3D printed samples

Task 2.6 Interlayer bond improvement

The interlayer bond strength of the 3D-printed SHCC specimens was significantly lower than that in the in-layer direction, indicating pronounced material anisotropy associated with the layer-by-layer printing process. To address this limitation and improve interlayer bonding, two approaches were investigated: modifications to printing parameters and alterations to nozzle geometry.

Modifications of printing parameters

The first approach focused on modifying printing parameters, specifically the offset distance and feed rate, to enhance interlayer bonding. The offset distance, defined as the vertical movement of the nozzle in the z-direction between successive layers, was varied to control interlayer contact and compression. Specimens were printed using three different offset distances: (i) 4 mm, (ii) 8 mm, and (iii) 12 mm. For each offset distance, the feed rate, corresponding to the material extrusion rate, was adjusted to maintain print stability and adequate buildability.

After printing, the specimens were cut into test coupons and prepared for tensile testing to quantify interlayer bond strength. Visual inspection of the printed specimens revealed that samples produced with a 12 mm offset distance exhibited poor surface texture, inadequate layer cohesion, and reduced print quality. Consequently, specimens printed with a 12 mm offset distance were excluded from further mechanical testing. Figure 22 presents representative surface textures and print quality associated with the different offset distances.

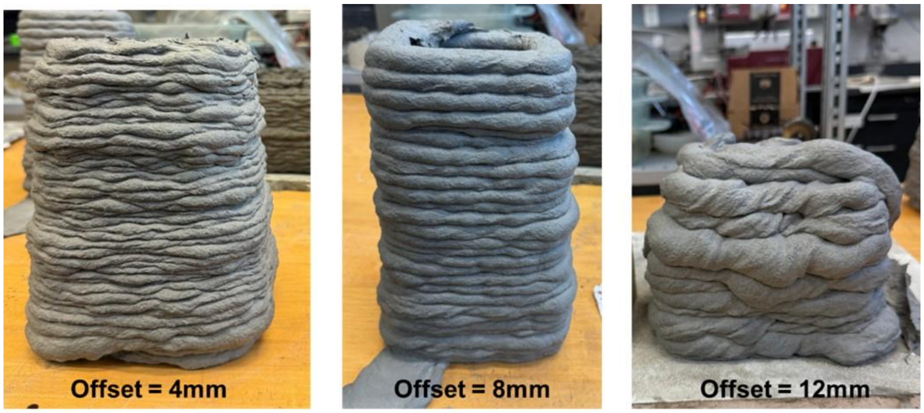

Figure 22. Printed layers with different offset distances

Use of grooved nozzles

The second approach investigated the use of grooved nozzles to improve interlayer bond strength. Unlike conventional flat nozzles, the grooved nozzles were designed to intentionally roughen the top surface of each deposited layer, thereby enhancing mechanical interlocking between successive layers. Specimens printed using grooved nozzles were produced under otherwise identical printing conditions and were compared directly with specimens printed using flat nozzles. The effectiveness of this approach was evaluated through mechanical testing of interlayer bond strength. Figure 23 illustrates the geometry of the grooved nozzle in comparison with the flat nozzle used for baseline printing.

Figure 23. Printed layers with different nozzles

Task 2.7 Durability evaluation

Durability evaluation was performed to assess the influence of mechanically induced surface crack patterns on the corrosion behavior of embedded steel reinforcement in cylindrical specimens described above. Particular emphasis was placed on comparing conventional reinforced concrete specimens with and without protective covers after mechanical loading. Accelerated corrosion testing (ACT) was employed to simulate the corrosion propagation phase within a shortened experimental timeframe and to evaluate how crack morphology and crack confinement affect corrosion progression. The experimental methodology was adapted from established potentiostatic accelerated corrosion procedures reported in the literature [29].

All specimens subjected to accelerated corrosion testing were first mechanically loaded to induce cracking representative of service-level damage, as described above in Task 2.3. The mechanical loading created visible surface cracking, after which the specimens were unloaded and visually inspected. Following the mechanical loading, no repair or crack sealing was performed and the specimens were allowed to stabilize under wet conditions for 24 hours to eliminate transient moisture effects. The exposed steel reinforcement was electrically connected to enable controlled electrochemical corrosion during the accelerated testing phase.

Accelerated corrosion testing methodology

Accelerated corrosion tests were conducted using a potentiostatic macro-cell corrosion setup, in which an external electrical potential of 10 volts was applied to drive corrosion of the embedded reinforcement. This method accelerates the transport of ionic species and promotes anodic dissolution of steel, allowing corrosion-induced damage mechanisms to be examined within a practical laboratory timeframe. The ACT targets explicitly the corrosion propagation phase, which is most sensitive to crack width, crack connectivity, and cover integrity.

Electrochemical configuration

In each specimen, the embedded steel reinforcement served as the anode, while an external stainless-steel mesh wrapped around the specimen surface functioned as the cathode. A direct current (DC) power supply was used to apply a constant electrical potential between the anode and cathode. Electrical connections were carefully insulated to prevent unintended current leakage or short-circuiting. To prevent preferential corrosion at exposed bar ends, all protruding reinforcement was coated with epoxy before testing, ensuring that corrosion was localized to the embedded region of the specimen.

Exposure environment and wet–dry cycling

Chloride exposure was provided using polyurethane sponges saturated with a 5% by weight sodium chloride (NaCl) solution and wrapped circumferentially around the specimens. The salt concentration was selected to represent an aggressive chloride environment capable of sustaining corrosion activity throughout the test duration.

Rather than continuous immersion, a cyclic wetting–drying regime was employed. The sponges were periodically rewetted with the salt solution at 24-hour intervals, followed by partial drying under laboratory conditions. This exposure protocol was selected to simulate field-relevant conditions, in which alternating access to moisture and oxygen governs corrosion kinetics. The wet-dry cycles also promote repeated ingress of chlorides through existing cracks, making the test particularly sensitive to crack width. The ACT setup used in this study is shown in Figure 24.

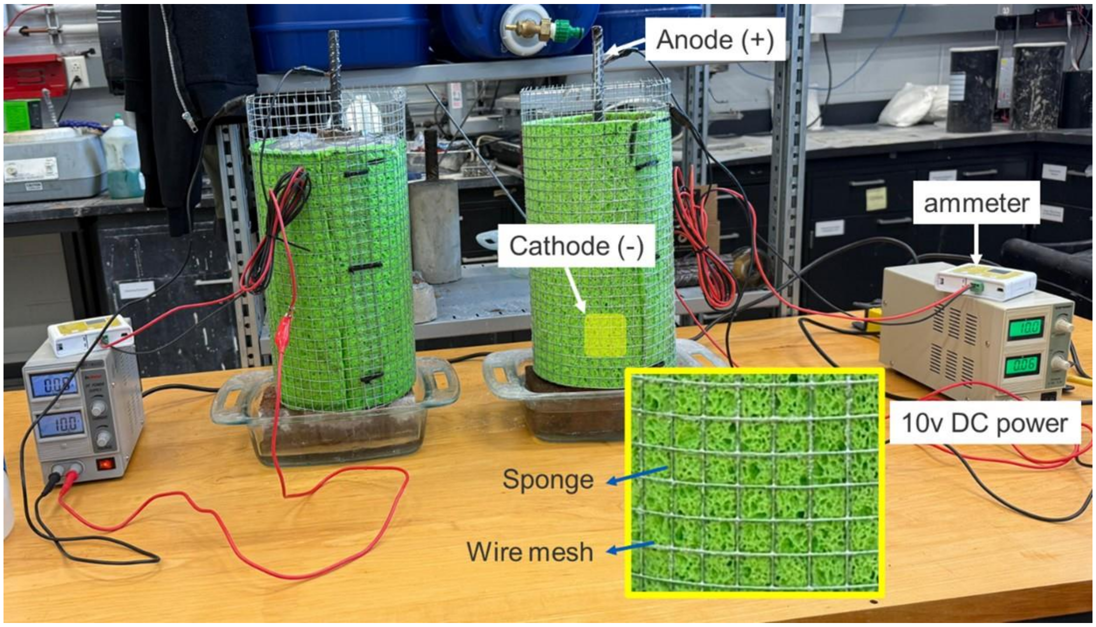

Figure 24. Accelerated corrosion test setup

Monitoring and test duration

The corrosion process was monitored by recording anodic current throughout the test. The applied electrical potential was constantly maintained at 10 volts, and the resulting current response was continuously logged. The magnitude and evolution of the anodic current provided a qualitative indicator of corrosion activity and ionic transport through the cracked concrete cover. Testing was continued for a predefined duration of 1000 hours for the monolithic concrete cylinder without cover and 400 hours for the composite cylinder with printed SHCC cover, sufficient to induce measurable corrosion-related damage while maintaining the structural integrity of the specimens for post-test examination.

Post-processing and analysis of results

The anodic current recorded during the accelerated corrosion tests was integrated over time of exposure to estimate reinforcement mass loss based on Faraday's Law of Electrolysis. The estimated mass loss served as a quantitative indicator of corrosion. It was used to compare the relative severity of corrosion between monolithic and composite specimens.

Upon completion of the accelerated corrosion tests, the specimens were carefully dismantled to retrieve the embedded steel reinforcement. The extracted reinforcement was cleaned to remove corrosion products using standardized chemical cleaning procedures in accordance with ASTM G1 [38]. This procedure ensured the removal of corrosion products without significant loss of base metal, enabling accurate determination of the remaining steel mass.

The cleaned reinforcement was subsequently dried and weighed, and the measured post-test mass was compared with the pre-test mass to determine the actual mass loss due to corrosion. The experimentally observed mass loss was evaluated alongside the electrochemically estimated mass loss derived from anodic current integration. This comparison provided insight into the effectiveness of the accelerated corrosion methodology and enabled assessment of the influence of cracking on corrosion propagation.

Task 2.8 Mechanical testing of beams

The experimental program was designed to investigate the shear and flexural behaviors of reinforced concrete (RC) beams with and without SHCC covers. A total of four RC beams with identical overall outer dimensions of 8"x8"x40" were cast and tested. Of these four beams, two were monolithic, made entirely of conventional concrete (without SHCC cover), and the other two were composite, also made of conventional concrete but with printed SHCC cover in the maximum flexure and shear zones. One of the two monolithic beams was designed to fail first in flexure, whereas the other was designed to fail first in shear. Similarly, the two composite beams were designed to fail in flexure and shear. The geometry, loading configuration, and reinforcement detailing for the composite beams are shown in Figure 25.

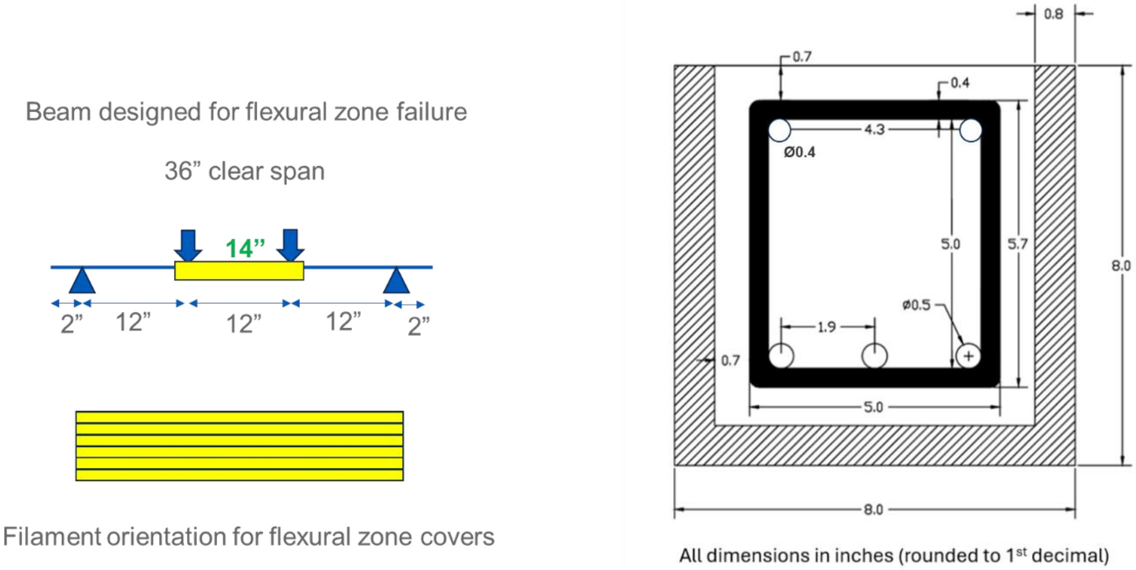

(a) Flexure-critical beam

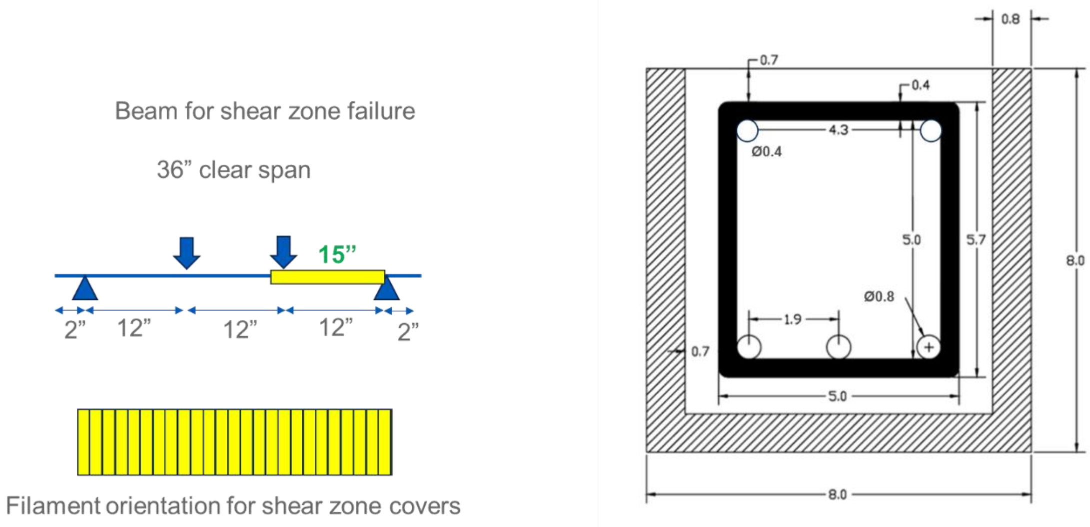

All dimensions in inches (rounded to 1st decimal)

(b) Shear-critical beam

Figure 25. Geometry, loading, and reinforcement detailing of reinforced concrete beams

The flexure-critical beams were designed to yield before concrete crushing. As shown in Figure 25(a), these beams had three #4 rebars in the bottom tensile zone. Two #3 rebars were used at the top of the beam to hold the stirrups in place. The shear stirrups were #3 rebars placed at a center-to-center spacing of 3”. This resulted in a design shear to flexural capacity ratio of 2.3 based on ACI 318-19 [39]. The printed SHCC covers, 14” in length, were placed at the mid-span of these beams as shown in Figure 25(a).

The shear-critical beams were designed to fail in a brittle mode to observe the effect of SHCC covers in mitigating such failure and achieving crack width control. These beams had a higher reinforcement ratio in the flexural zone to reduce the likelihood of flexural failure, and no shear reinforcement to facilitate shear failure. The design shear to flexural capacity ratio for these beams was 0.33 based on ACI 318-19 [39], increasing the likelihood of shear failure. Additionally, the loading was altered as shown in Figure 25(b) to increase the probability of shear failure. The printed SHCC cover was placed in the maximum shear zone of one of the end spans. The overall length of the cover used in the shear zone was 15”.

The beams were tested under a four-point loading setup using a servo-hydraulic actuator, with pin-roller end supports providing simply-supported boundary conditions. Loading was applied incrementally under displacement control, with intermediate stoppages every 2 mm of actuator displacement to observe cracks and measure crack counts and widths. Midspan deflection and support rotations were measured with linear potentiometers. Strains in the longitudinal rebars were monitored using strain gauges installed on the rebars prior to concrete casting.

The test data were recorded using a synchronized data-acquisition system, enabling the computation of load-deflection characteristics, stiffness degradation, ductility indices, and energy absorption. Figure 26 shows the test setup and instrumentation details for reinforced concrete beams. The measured ultimate moments and shear capacities were subsequently compared with theoretical predictions from sectional analysis and current design code provisions to assess the structural implications of 3D-printed SHCC covers.

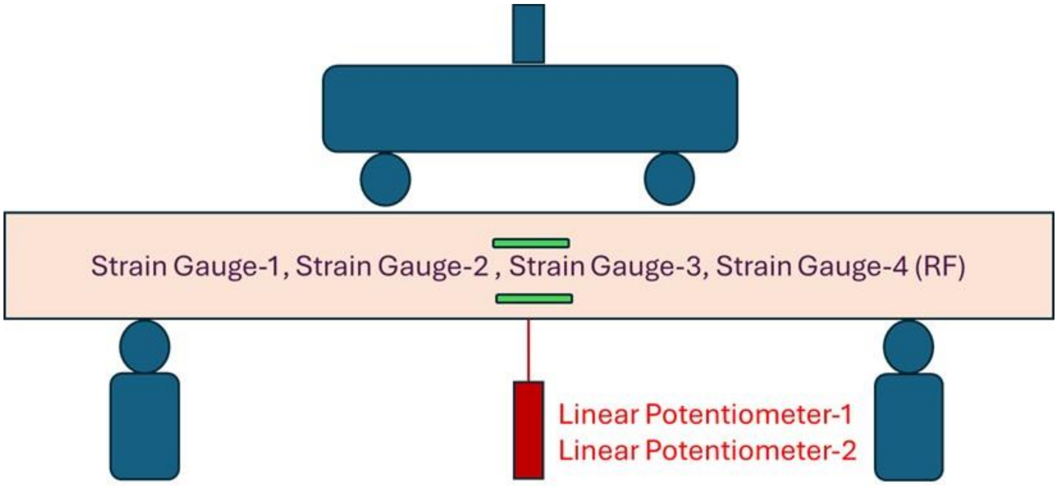

Figure 26. Test setup and instrumentation details for reinforced concrete beams

The mixture proportions for concrete and SHCC are given in Table 4. Type IL Portland-limestone cement conforming to ASTM C595 [40] was used for concrete. Natural river sand with a fineness modulus of 2.7 served as fine aggregate, and crushed limestone with a maximum nominal aggregate size of 0.5" was used as coarse aggregate. Potable tap water was used for mixing and curing. Concrete mix design was proportioned for a target 28-day compressive strength of 6 ksi, determined using trial mixes and adjusted for workability based on slump tests performed in accordance with ASTM C143 [34]. The water/cement ratio was maintained at 0.35, and a Type F (ASTM C494 [68]) polycarboxylate ether-based high-range water-reducing admixture (HRWRA) was added at 0.35% by weight of cement to ensure adequate workability. Concrete batches were prepared in a 3.5 cft gravity mixer in accordance with ASTM C192 [41].

The 3D-printable SHCC consisted of Type IL cement, class F fly ash conforming to ASTM C618 [42], fine silica sand (F-75), ground silica with a median and maximum particle sizes of 3 μm and 10 μm, respectively, Type F (ASTM C494 [43]) polycarboxylate ether-based HRWRA, and Type S (ASTM C494 [43]) Viscosity Modifying Admixture (VMA). Polyvinyl alcohol (PVA) microfibers with a length of 8mm and a diameter of 38μm were used in SHCC. The SHCC mixture was prepared in a 30-qt planetary mixer. All the solid ingredients were first dry-mixed for three minutes. After that, water, HRWRA, and VMA were added and mixed for another 5 minutes at a paddle speed of 100-120 rpm. Subsequently, fibers were added, and the mixing was continued for another five minutes at paddle speed of 180-200 rpm to achieve a homogeneous fiber dispersion.

Grade 60 (ASTM A615 [44]) deformed steel bars were used for both tension and compression reinforcement.

Table 4. Mixture proportions (by weight) for concrete and 3D-printable SHCC

MATERIAL	Cement (Type IL)	Fly Ash (F)	Sand (F-75)	Coa-rse Agg	Fine Agg	Ground silica (Min-u-sil 10)	HRWRA (ADVA-190)	VMA	Water	PVA fiber
Concrete	1	-	-	2.0	1.6	-	0.35% cement wt.	-	0.35	-
3D-printable SHCC	1	1.2	0.78	-	-	0.041	0.33% binder* wt.	1.5% binder wt.	0.68	2% by vol.

* binder = cement + fly ash

For preparing the composite beams, the SHCC covers were first printed, as shown in Figure 27(a). 3D printing of SHCC results in material anisotropy, such that the tensile strength and strain capacity are the highest along the printed filaments. Given this, the SHCC filaments were printed parallel to the flexure-critical beam's longitudinal axis. The most desirable orientation for shear strengthening is 45 degrees relative to the longitudinal axis. However, it is more convenient to print a cover with filaments perpendicular to the beam length, like stirrups. Therefore, the SHCC cover for the shear-critical beam was printed as shown in Figure 27(a).

A small-scale gantry-type 3D printer was employed to print the covers. The outer cross-section of the cover was equal to the outer dimension of the beam, i.e., 8″ x 8″. Once printed, these covers were placed in the respective beam's forms at the locations (marked in yellow) shown in Figure 25. The beam molds with the printed covers are shown in Figure 27(b). After that, the reinforcement was placed inside the formwork as shown in Figure 27(b). Next, concrete was poured and cured for 14 days in a moist condition, at which point the formwork was removed, and the beams were instrumented for testing.

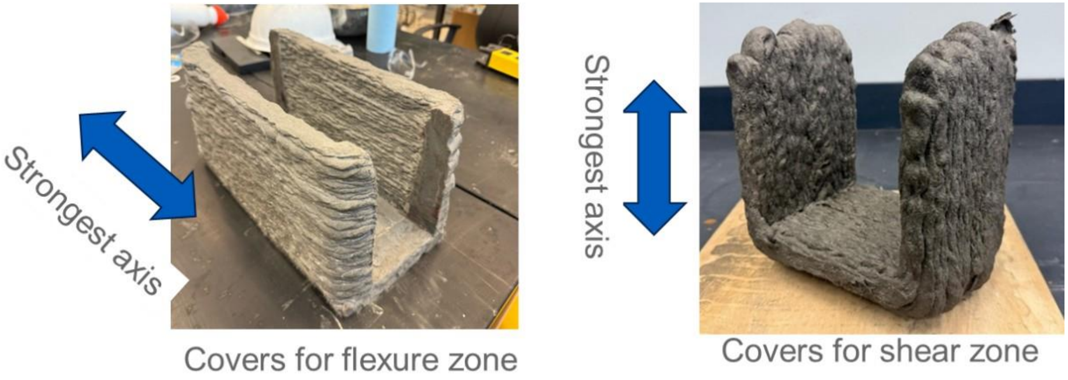

(a) Step 1: Printing of SHCC covers

(b) Step 2: Placement inside formwork

(c) Step 3: Concrete Pour

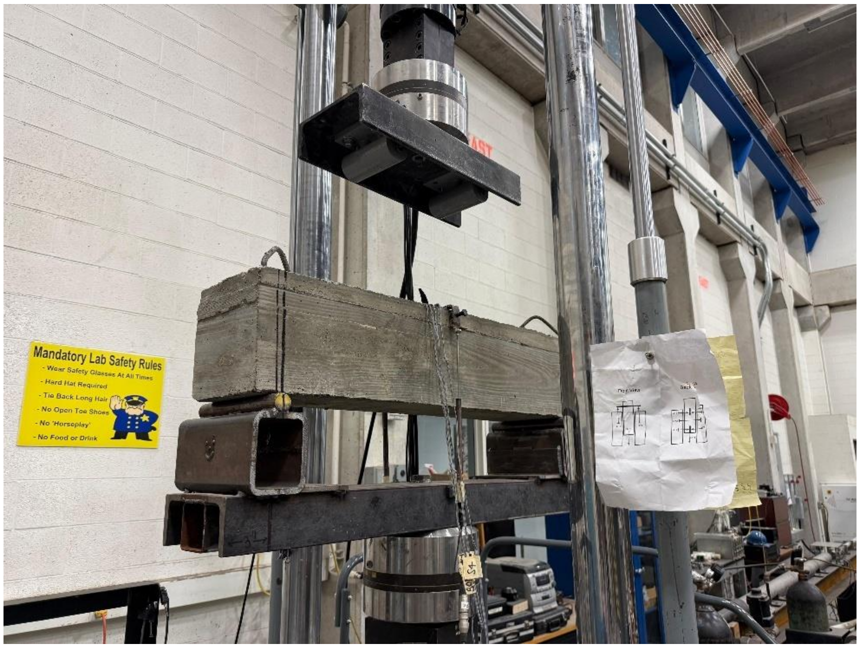

(d) Step 4: Testing

Figure 27. Preparation and testing of composite beams

Task 2.9 Printer optimization

The small-scale 3D concrete printer developed in Year 1 was enhanced and optimized to improve the fabrication of SHCC covers. The printer optimization in Year 2 focused on achieving stable extrusion, consistent filament geometry, and sufficient buildability to support multi-layer printing of SHCC elements. Modifications were implemented sequentially, and their performance was evaluated through iterative printing trials to achieve the desired print quality for SHCC cover fabrication.

Extrusion Rate Control

Extrusion rate control was identified as a critical requirement due to variations in rheological properties among different 3D-printable SHCC mixtures. Adjustable extrusion rates were achieved through differential hopper feeding and controlled hopper vibration, enabled by a flexible hopper support. This configuration allowed the printer to accommodate mixtures with varying flowability while maintaining stable extrusion. Using this approach, sufficient buildability was achieved to print a 12-inch-high cylindrical specimen without loss of shape stability, demonstrating the potential for further height extension if required. 3D-printed cylindrical samples with varying feed rates and offset distances are shown in Figure 28.

Mix 10
F.R. = 8000
O.D. = 4mm

Mix 9I
F.R. = 8000
O.D. = 4mm

Mix 9I (1hr)
F.R. = 3000
O.D. = 4mm

Figure 28. Buildability enhancement by extrusion rate control (F.R.= Feed Rate, O.D. = Offset Distance)

Control of Cover Thickness

Variations in mixture flowability resulted in observable changes in filament width and layer thickness during printing. To achieve the desired SHCC cover thickness, the nozzle diameter was adjusted, and the extrusion rate and nozzle travel speed were optimized. This approach enabled consistent filament deposition and improved dimensional control, particularly when printing with smaller nozzle diameters. The optimized combination of nozzle size, extrusion rate, and nozzle movement resulted in improved surface quality and uniform cover thickness, as shown in Figure 29.

Nozzle diameter = 20 mm (0.8")
Cover thickness = 30 mm (1.2")

Nozzle diameter = 15 mm (0.6")
Cover thickness = 20 mm (0.8") - ok

Figure 29. Filament width reduction with a reduction in nozzle diameter

5. Project results

Year 1

- The numerical analysis in Task 1.1 estimated that the maximum tensile strain on the girder end surface was 0.32%. Additionally, the analysis indicated that a 0.75″ thick SHCC cover did not significantly affect the tensile stress in the longitudinal reinforcement within the anchorage zone.

- Tasks 1.1 and 1.2 resulted in the determination of target material properties for developing 3D-printable SHCC as follows:

  Fresh properties (flow table test):

  i. Flowability factor (slump diameter after 25 drops/original diameter) = 1.2 to 1.5; for a nozzle size ≥ 0.76”
  ii. Flow reduction rate (average percentage decrease rate in flowability factor in first 30 min) > 20% per hour

  Hardened properties:

  i. Uniaxial compressive strength > 6 ksi
  ii. Uniaxial tensile strain capacity > 0.6%

- Task 1.3 led to the development of three feasible SHCC mixtures with good printability.

- In Task 1.4, the hardened properties of these three mixtures were determined using conventional mold-cast specimens, which are summarized in Table 5. Representative tensile stress-strain behaviors and bending stress-deflection response for mixtures M9-MS, M9-IS, and M10 are shown in Figures 30 and 31, respectively.

Table 5. Hardened properties of 3D printable SHCC mixtures (COV = coefficient of variation)

Mix	Compressive strength		Tensile strength (Direct tension test)		Modulus of rupture (4-point bend test)	
	Mean (ksi)	COV (%)	Mean (ksi)	COV (%)	Mean (ksi)	COV (%)
M9-IS	7.5	5.6	0.8	19.0	1.5	12.5
M9-MS	8.5	2.4	0.7	17.5	1.5	8.0
M10	8.2	5.6	0.9	15.1	1.3	8.4

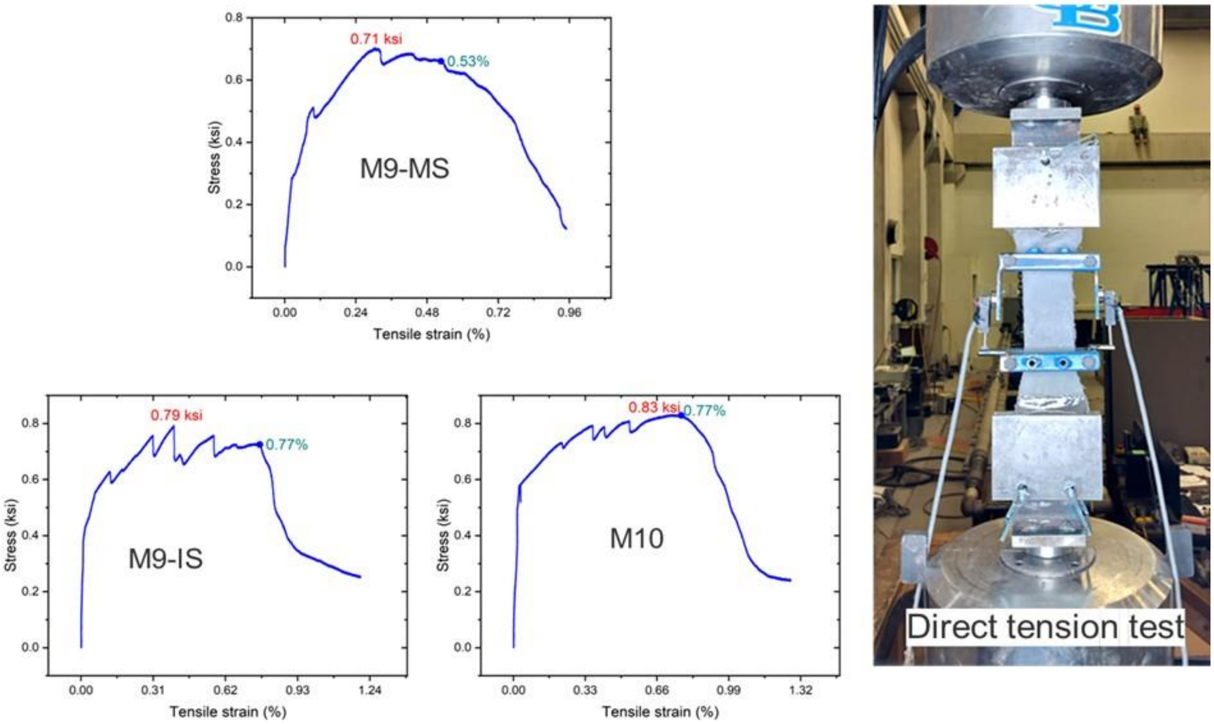

Figure 30. Stress-strain response of 3D printable SHCC mixtures under direct tension

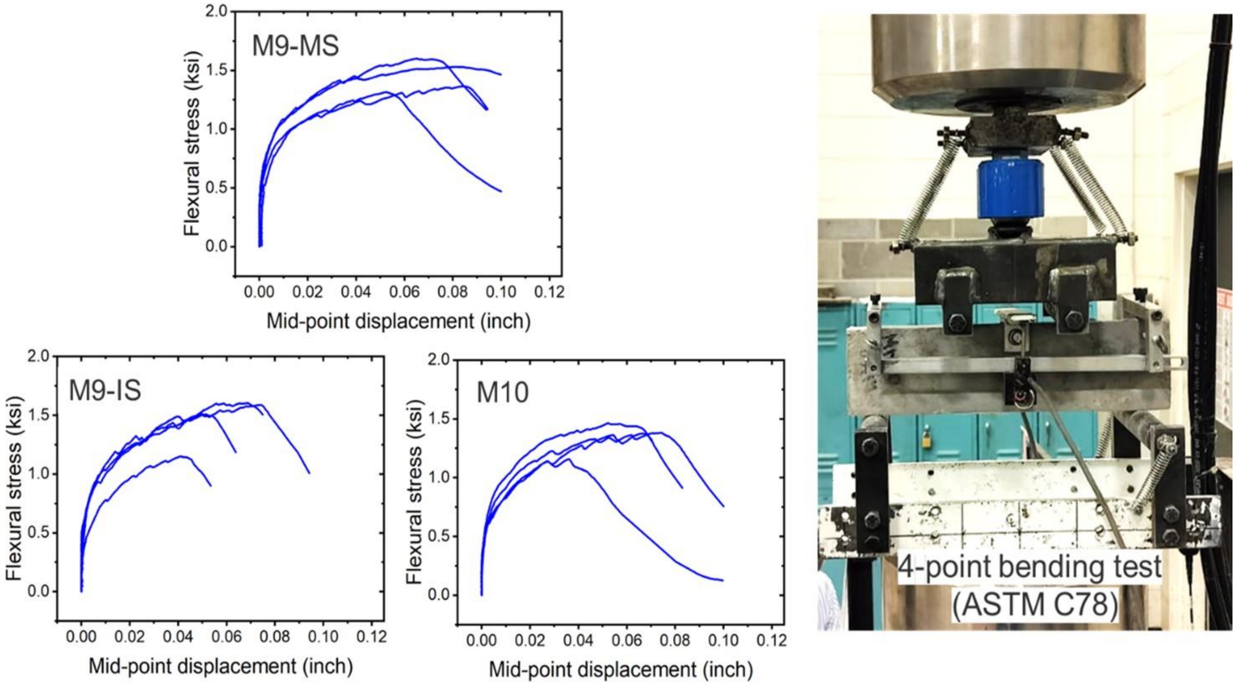

Figure 31. Flexural stress-midpoint deflection response of 3D printable SHCC mixtures under four-point bending

- Task 1.5 investigated the effect of increasing the fly ash content on the hardened properties of the SHCC mixtures. Although a marginal decline in 28-day compressive strength was observed with increase in fly ash content, the tensile strain capacity showed an increasing trend with increased fly ash content. However, the variation in results (COV) was too high to draw definitive conclusions. Although an elaborate quantification of the flow behavior was not performed, it was observed that the mix flowability was too high for the fly ash/cement weight ratio of 1.8, indicating the need for rheological re-optimization for 3D printing application at such a high proportion of fly ash in the mixture. Considering the need for rheological re-optimization, the modified mixtures were not used further in this research. Table 6 summarizes the hardened state properties of the modified 3d printable SHCC mixture.

Table 6. Hardened properties of modified 3D printable SHCC mixtures

SHCC Mix	Fly ash to cement weight ratio	Compressive strength		Tensile strength (from direct tension test)		Tensile strain capacity	
		Mean (ksi)	COV (%)	Mean (ksi)	COV (%)	Mean (%)	COV (%)
M9-IS	1.2 (Base)	7.5	5.6	0.8	19.0	0.7	22.6
	1.5	6.4	12.8	0.7	4.8	1.4	17.4
	1.8	6.3	12.5	0.7	2.0	2.1	17.2
M9-MS	1.2 (Base)	8.5	2.4	0.7	17.5	0.6	27.0
	1.5	8.7	6.8	0.9	1.3	1.3	23.1
	1.8	8.1	6.9	1.0	8.3	1.9	47.4
M10	1.2 (Base)	8.2	5.6	0.9	15.1	0.9	58.3
	1.5	7.2	5.1	0.9	5.6	1.7	10.2
	1.8	6.3	1.5	0.8	1.2	1.9	14.1

- In Task 1.6, flexural testing of a monolithic concrete beam (without SHCC covers) showed substantial cracking in the flexural zone. This beam exhibited pronounced flexural cracks that localized and widened with increasing load, ultimately governing the failure behavior. In contrast, the composite beam incorporating SHCC covers exhibited negligible surface cracking within the flexural zone protected by the cover, demonstrating the effectiveness of the SHCC shell in suppressing cracks at the external surface.

  The load capacities of the monolithic and composite beams were 28.7 kip and 25.8 kip, respectively. Although the composite beam with the SHCC cover exhibited a slightly lower ultimate load, the observed failure modes differed significantly between the two configurations. The monolithic beam failed in a flexure-dominated mode, characterized by extensive cracking and damage in the tensile zone. On the other hand, the composite beam did not fail in the span covered by the printed SHCC cover; instead, failure occurred outside the covered zone and was governed by shear cracking. These results indicate that the SHCC cover provided sufficient crack control and did not significantly reduce the flexural capacity. The cracked beams with residual cracks are shown in Figures 32 and 33 post-testing.

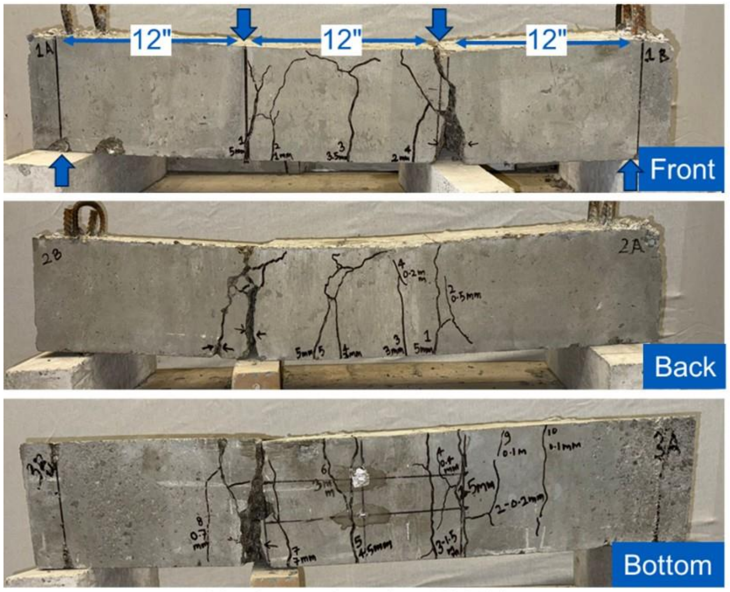

Maximum Load = 28.7 kip
(0.5″ mid-point displacement)

Figure 32. Post-testing residual cracks in the monolithic beam

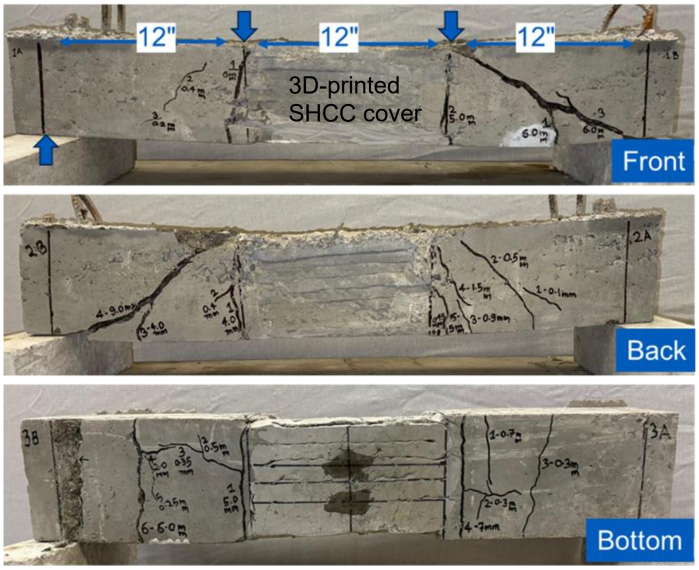

Maximum Load = 25.8 kip
(0.4″ mid-point displacement)

Figure 33. Post-testing residual cracks in the composite beam

- Post-test chipping of the SHCC cover revealed no evidence of delamination between the SHCC shell and the conventional concrete substrate (Figure 34). The interface remained intact, confirming effective composite action between the cover and the concrete core. Furthermore, no cracking was observed in the SHCC cover or at the concrete surface beneath it. These observations show the feasibility of the proposed concept of using 3D-printed SHCC covers to control surface cracking and improve durability in prestressed and reinforced concrete applications, warranting further investigation and optimization.

Figure 34. Composite beam after removal of 3D-printed SHCC cover

Year 2

- The axial pull-off tests in Task 2.1 yielded an average bond strength of 0.16 ksi with a coefficient of variation (COV) of 21%. All specimens failed at the SHCC–concrete interface, confirming that the measured value corresponds to the axial tensile bond capacity between SHCC and conventional concrete. The shear bond tests in Task 2.1 showed an average bond strength of 0.17 ksi with a coefficient of variation (COV) of 13%. Failure consistently occurred along the SHCC–concrete interface, indicating that the measured strength represents the shear bond capacity of the interface.

- The numerical analysis in Task 2.2 yielded distinct bond strength requirements for axial tension and shear at the concrete–SHCC interface. The required bond strength in axial tension was calculated to be 0.07 ksi (0.5 MPa), indicating a relatively modest demand for maintaining composite action in tension. In contrast, the calculated shear bond strength was significantly higher, at 0.61 ksi (4.2 MPa), reflecting the dominant role of shear transfer at the interface. These results indicate that shear governs the bond design between conventional concrete and SHCC covers. The predicted bond strength requirements obtained from the numerical analysis were subsequently used as benchmarks for evaluating experimentally measured bond strengths and assessing the effectiveness of bond modification strategies.

- In Task 2.3, mechanical testing of monolithic and composite cylindrical specimens was conducted to compare their cracking characteristics. Figure 35(a) shows that there were two types of cracks in the monolithic specimen (without SHCC cover): (i) splitting cracks localized near the ends of the embedded reinforcement, and (ii) transverse tensile cracks perpendicular to the embedded rebar. The splitting cracks at the reinforcement embedment regions dominated the failure process and were accompanied by significant concrete fragmentation, while the transverse tensile cracks contributed to rapid loss of specimen integrity. Together, these cracks indicate a brittle cracking response in conventional concrete specimen.

- The composite cylindrical specimen incorporating a 3D-printed SHCC cover effectively prevented post-peak disintegration of the concrete core following maximum load application. Figure 35(b) shows no major splitting cracks, indicating that the SHCC cover provided effective confinement and crack control. Only microcracks were observed near the reinforcement at the specimen ends, as SHCC effectively confined these microcracks and prevented their propagation to the surface. However, due to reduced interlayer bond strength and inherent material anisotropy associated with the layer-by-layer 3D printing process, transverse cracking within the SHCC cover tended to localize along the weakest interlayer plane. Despite this localized cracking, the overall integrity of the specimen was maintained, and catastrophic fragmentation was avoided.

- In the monolithic reinforced concrete cylinder, four transverse surface cracks were identified, with crack widths ranging from approximately 0.6 mm to 5.5 mm. In contrast, the composite specimen with a printed SHCC cover exhibited only one transverse surface crack of 6.5 mm width.

- Post-test inspection revealed that the SHCC covers remained intact and well-adhered to the underlying concrete. Cracks observed on the SHCC surface did not propagate into large separations at the SHCC-concrete interface. No signs of cover debonding, delamination, or spalling were observed.

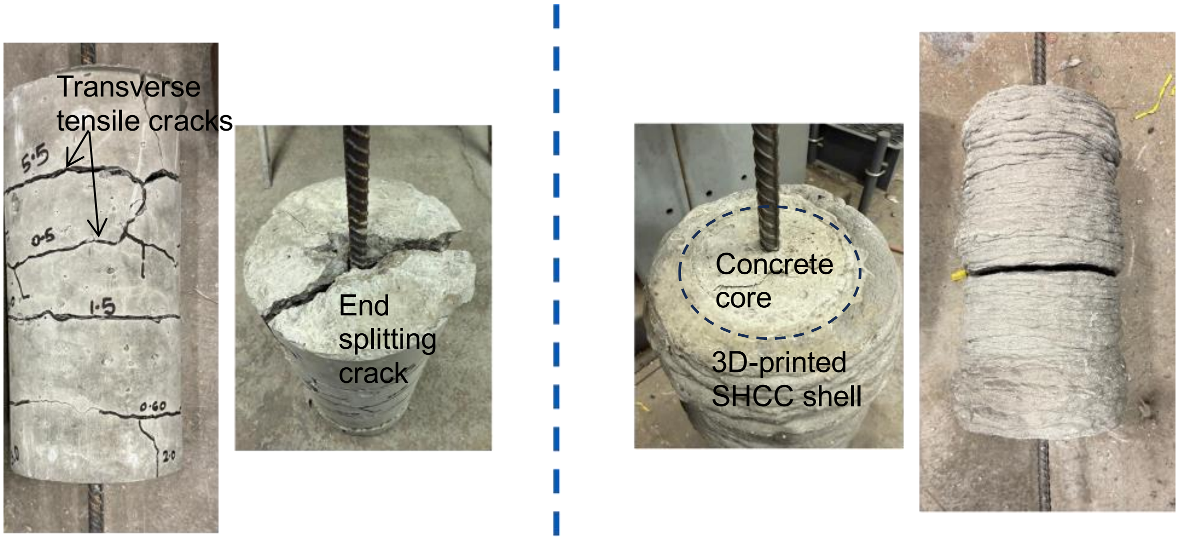

(a) Monolithic specimen

(b) Composite specimen

Figure 35. Cracking pattern in cylindrical reinforced concrete specimens

- In Task 2.4, surface modifications via 3D-printed grooves and sandblasting were investigated to increase shear bond strength. Two grooved specimens produced strengths of 0.19 ksi and 0.67 ksi, with an average of 0.43 ksi. Relative to the control specimen with a bond strength of 0.17 ksi, this represents a meaningful improvement in shear transfer capacity. However, the average value of 0.43 ksi remained below the required 0.61 ksi (notwithstanding one specimen that exceeded the requirement). In contrast, the specimens with both grooved and sandblasted interfaces produced lower strengths of 0.07 ksi and 0.13 ksi, with an average of 0.10 ksi, which was below the control value. This observation indicates that sandblasting, as implemented in this study, did not enhance the interface and likely reduced effective contact/mechanical interlock or introduced local damage/weakness at the interface.

- The interlayer bond strength of 3D-printed SHCC was evaluated in Task 2.5 using uniaxial tensile and split tensile testing methods. Results from the uniaxial tensile tests indicated an interlayer bond strength of 0.37 ksi, which corresponds to approximately 60% of the axial tensile strength of mold-cast SHCC specimens. This reduction highlights the influence of printing-induced anisotropy and the presence of weak interfaces between successive printed layers.

- The interlayer bond strength obtained from the split tensile tests was 0.47 ksi, corresponding to approximately 57% of the axial tensile strength of mold-cast SHCC specimens. The slightly higher bond strength measured in the split tensile configuration is attributed to differences in stress distribution and confinement effects inherent to the test geometry.

- To improve interlayer bond strength, the effects of printing parameters (offset distance and grooved nozzle) on interlayer bonding were evaluated in Task 2.6. Specimens printed with a 4 mm offset distance exhibited an average interlayer bond strength of 0.42 ksi, which was approximately 13% higher than the baseline value of 0.37 ksi determined in Task 2.5. The interlayer bond strength decreased with increasing offset distance. For specimens printed with an 8 mm offset distance, the average interlayer bond strength was only 0.34 ksi. The reduced bond strength at larger offset distance reflects diminished interlayer contact and weaker mechanical interaction between successive layers.

- Using a grooved nozzle with a 4 mm offset resulted in a substantial improvement in interlayer bond strength, with an average value of 0.68 ksi, 84% higher than the baseline. Although the interlayer bond strength achieved using the grooved nozzle remained lower than the axial tensile strength of cast and extruded-cast specimens, it significantly narrowed the performance gap introduced by the printing process.

- Durability of reinforced concrete cylindrical specimens (both monolithic and composite) subjected to accelerated corrosion was evaluated in Task 2.7. These specimens underwent mechanical loading in Task 2.3, which resulted in different cracking patterns in monolithic and composite specimens, as discussed above. The results of accelerated corrosion test are presented below in terms of crack observations, anodic current–time response, theoretically estimated reinforcement mass loss, and experimentally measured reinforcement mass loss.

- At the end of the accelerated corrosion, the monolithic concrete specimens exhibited severe corrosion. As these specimens were already cracked significantly before accelerated corrosion (due to mechanical loading in Task 2.3), no additional corrosion-induced cracks were observed. In contrast, specimens incorporating SHCC covers showed markedly improved performance. No corrosion-induced cracks were observed during or after the accelerated corrosion exposure. This behavior is attributed to the ductile SHCC cover, which absorbed the tensile pressure generated by expanding rust products without forming corrosion-related cracking at the external surface. As a result, the overall structural integrity of the SHCC-covered specimens was maintained throughout the durability testing. Figure 36 shows the specimens after accelerated corrosion testing.

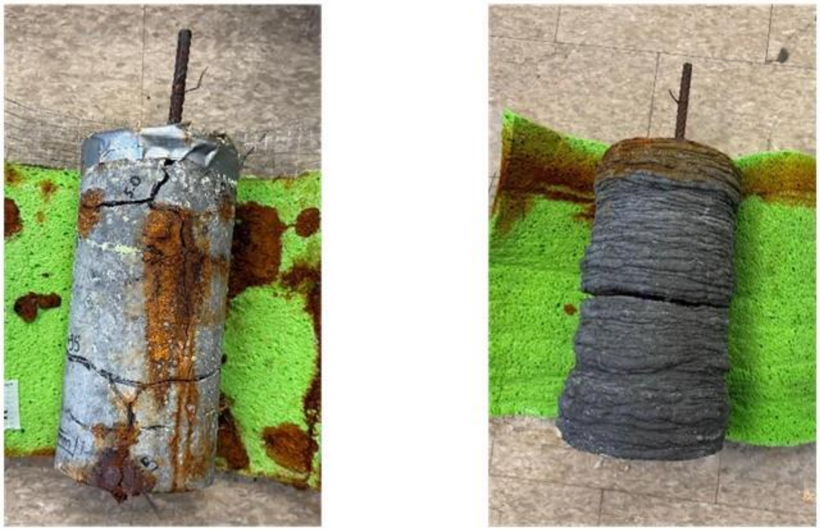

(a) Monolithic specimen (b) Composite specimen

Figure 36. Specimens after accelerated corrosion testing

- The cracking behavior observed in the specimens was reflected in the anodic current–time response recorded during accelerated corrosion testing, as shown in Figure 37. Due to the presence of a single relatively wide crack in the composite specimen (with the printed SHCC cover), its initial anodic current was larger than that observed in the monolithic specimen (without the SHCC cover). However, as corrosion progressed, distinct differences emerged between the two systems. In the composite specimens, once the reinforcement in the cracking zone was corroded, the rust products around the rebar slowed its corrosion at that location. At the same time, the remaining regions of the rebar remained uncorroded as the SHCC cover effectively shielded them. This resulted in a pronounced reduction in the composite specimen's overall corrosion rate from approximately 100–200 mA to about 50 mA.

  In contrast, the monolithic specimen exhibited sustained corrosion activity throughout the test duration. Excluding transient current peaks associated with periodic electrolyte rewetting, the anodic current for these specimens fluctuated consistently around 100 mA. Although the rust products slowed corrosion at a given rebar location (similar to the composite specimen), new corrosion sites likely continued to initiate during the accelerated corrosion of the monolithic specimen. The absence of effective crack confinement allowed continued access of chlorides and moisture to the reinforcement, leading to persistent corrosion across a larger portion of the embedded steel.

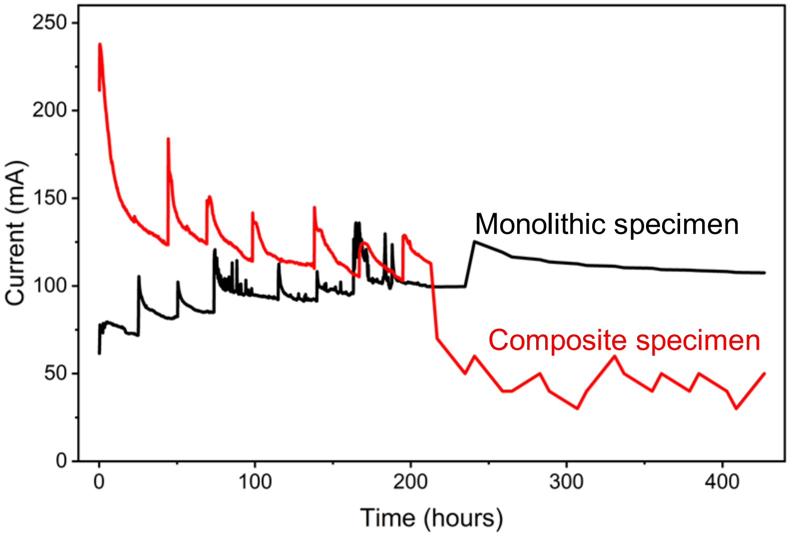

Figure 37. Anodic current-time plot from accelerated corrosion testing

- The area under the anodic current–time response was used to theoretically estimate reinforcement mass loss using Faraday’s Law of Electrolysis. In monolithic specimens, after 200, 400, and 1000 hours of accelerated corrosion testing, the calculated mass loss was approximately 5%, 11%, and 32% of the original reinforcement mass, respectively. These values indicate continuous and widespread corrosion activity enabled by unconfined cracking and direct exposure of the reinforcement to aggressive species.

  In composite specimens, the calculated reinforcement mass loss after 200 and 400 hours of accelerated corrosion testing was approximately 6% and 9%, respectively. The reduced rate of mass loss was consistent with the observed decline in anodic current. It reflected the SHCC cover's ability to confine cracking and limit corrosion beyond the immediate cracked region.

- The experimentally measured reinforcement mass-loss results were evaluated against theoretical estimates derived from anodic current integration. For the monolithic specimens, the experimentally observed reinforcement mass loss after 1000 hours of accelerated corrosion testing was approximately 25% of the original rebar mass. The corresponding theoretical estimate, derived from anodic current integration over the same exposure duration, was 32%. The discrepancy can be attributed to inefficiencies inherent in accelerated corrosion testing, such as partial diversion of impressed current to side reactions, nonuniform current distribution along the reinforcement, and loss of corrosion products during exposure and specimen handling, all of which can lead to overprediction of mass loss by electrochemical methods.

  For the composite specimens incorporating 3D-printed SHCC covers, the experimentally measured reinforcement mass loss was approximately 14% after 400 hours of accelerated corrosion testing, compared to a theoretical estimate of 9% for the same duration. In this case, the experimentally observed mass loss exceeded the theoretical prediction. This behavior is consistent with the localized nature of corrosion in SHCC-covered specimens, where corrosion activity was concentrated near dominant crack locations.

It is also important to note that the experimental results correspond to different exposure durations for the two specimen types. The monolithic specimens were evaluated after 1000 hours, whereas the composite specimens were evaluated after 400 hours of accelerated corrosion. This was due to an unexpected data loss beyond 400 hours. Figure 38 shows the extracted rebar condition in both the specimens after accelerated corrosion testing.

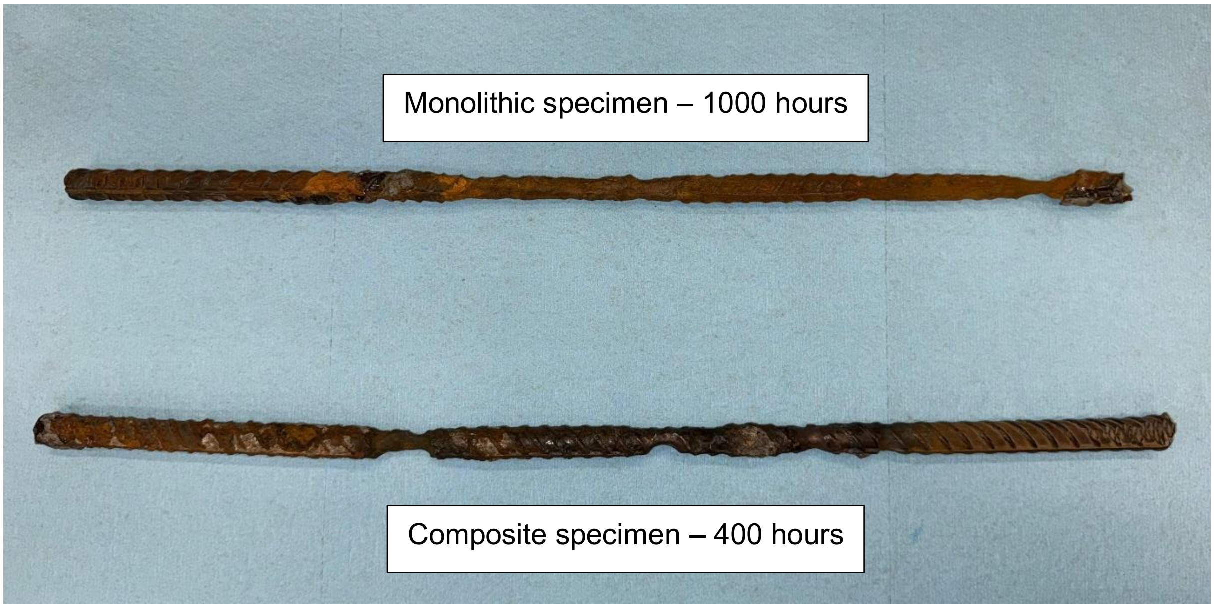

Figure 38. Extracted rebar condition after accelerated corrosion test

- Task 2.8 involved testing four reinforced concrete beams (1) Flexure-critical monolithic (control) beam, (2) Flexure-critical composite beam, (3) Shear-critical monolithic (control) beam, and (4) Shear-critical composite beam. Figure 39 presents the load-deflection (at mid-span) responses for flexure-critical beams. Both the specimens (monolithic and composite) exhibited comparable elastic stiffness, as the two beams were largely made of the same material (except for the thin SHCC cover in the composite beam) and had identical dimensions. The observed failure loads in all the tested specimens exceeded the nominal flexural and shear capacities estimated using standard design procedures.

- The monolithic beam achieved a peak load of approximately 48 kip at a midspan deflection of about 15.5 mm. The composite beam with the SHCC cover in the middle span reached a peak load of approximately 38 kips at a midspan deflection of about 7.5 mm. The earlier termination of the composite beam is attributed to a shift in the failure mechanism, as discussed in the subsequent section. The load–displacement curves of both beams show several small load drops and subsequent recoveries. These fluctuations correspond to intentional loading pauses introduced during the test to measure surface crack widths, and do not indicate sudden loss of stiffness or instability in the structural response. Furthermore, neither flexure-critical beam failed in the middle maximum moment region; instead, failure initiated near the supports at load levels exceeding their estimated nominal capacities.

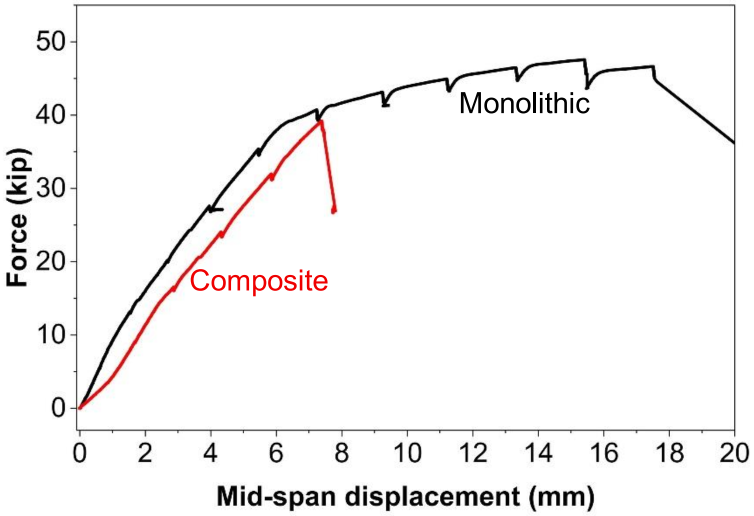

Figure 39. Load deflection behavior for beams designed to fail in flexure

- Figure 40 compares the load–deflection (at midspan) responses of the shear-controlled beams. Both beams exhibited similar linear response up to cracking, followed by stiffness reduction associated with the development of diagonal shear cracks. The monolithic beam developed diagonal cracking in the shear span, resulting in a peak load of approximately 39 kips and subsequent loss of load-carrying capacity.

- The composite beam achieved a slightly higher peak load of approximately 39.5 kips with a smoother post-cracking response. Importantly, failure in this specimen did not occur within the SHCC-covered shear zone. Instead, the diagonal cracking and eventual failure were observed in the portion of the beam outside the SHCC-covered region. Throughout the loading history, the SHCC-covered shear zone did not show any cracking at the external surface. No sudden stiffness loss or localized failure was observed within the SHCC region, indicating that the SHCC cover effectively protected the shear-critical zone from damage concentration.

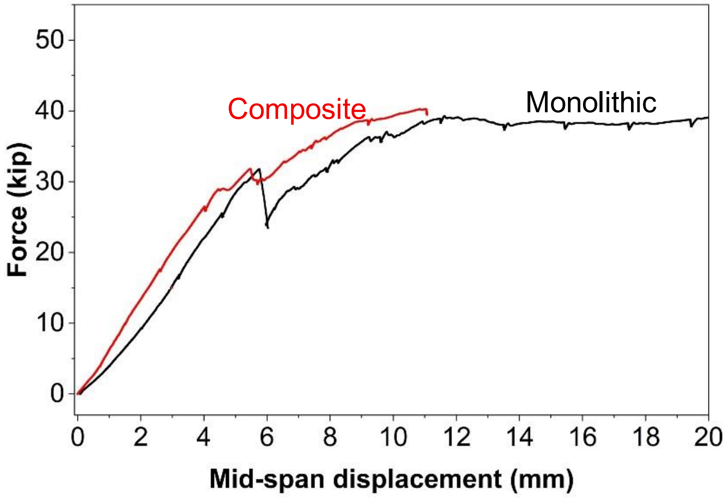

Figure 40. Load deflection behavior for beams designed to fail in shear

- Table 7 summarizes the crack widths recorded at discrete loading stages corresponding to 2 mm increments of actuator displacement. At each increment, visible surface cracks were counted, and their widths were measured at the bottom, mid, and top regions on both faces of the beam. For comparison, the maximum observed crack width and number of cracks at each displacement increment were summarized. No visible cracking was observed in the monolithic beam up to an actuator displacement of 4 mm (load = 13.2 kips). Major cracks first appeared at an actuator displacement of 6 mm (load = 20 kips), when three cracks were recorded with a maximum crack width of 0.30 mm. As the load increased, both the number of cracks and crack widths increased steadily. At the highest recorded actuator displacement of 12 mm (load = 40.1 kips), the monolithic beam exhibited extensive cracking, with 10 visible cracks and a maximum crack width of 1 mm, primarily within the midspan region. This indicates significant crack widening and localization before failure. The residual crack patterns for the tested flexure-controlled beams are shown in Figure 41.

Table 7. Crack development in flexure-critical monolithic beam

Actuator Displacement (mm)	Load (kips)	No. of Cracks	Max Crack Width (mm)
2	5.6	0	0
4	13.2	0	0
6	20	3	0.3
8	27.5	6	0.4
10	34.7	8	0.5
12	40.1	10	1

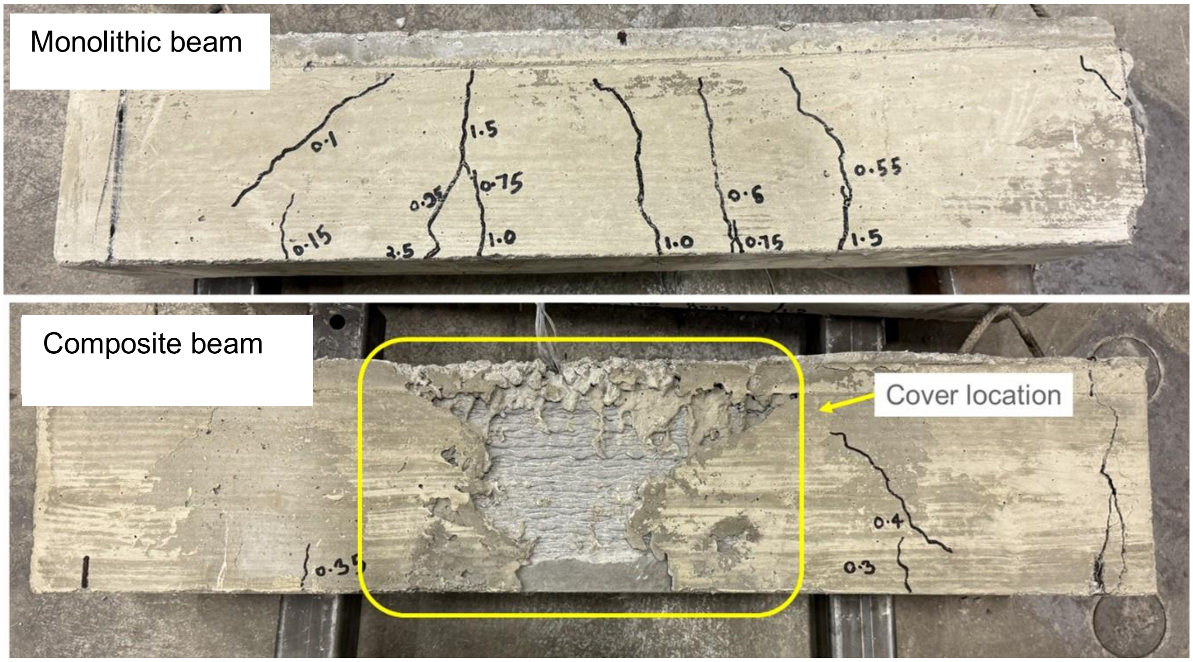

Figure 41. Post-testing residual crack pattern in flexure-critical beams

- Table 8 presents the crack development in the flexure-critical composite beam. No cracking was observed up to 4 mm actuator displacement (load = 9.3 kips). Initial cracking occurred at 6 mm displacement (load = 16.2 kips), with three cracks recorded and a maximum crack width of 0.30 mm. These cracks were located outside the SHCC-covered midspan region. At higher load levels, both crack number and widths increased, but none of the cracking occurred within the midspan. At the highest recorded actuator displacement of 12 mm (load = 39 kips), the beam exhibited 10 visible cracks with a maximum crack width of 0.60 mm.

Table 8. Crack development in flexure-critical composite beam

Actuator Displacement (mm)	Load (kips)	No. of Cracks*	Max Crack Width (mm)
2	3.6	0	0
4	9.3	0	0
6	16.2	3	0.3
8	23.7	5	0.4
10	31.9	8	0.5
12	39	10	0.6

*All cracks occurred outside the SHCC-covered mid span.

- Table 9 summarizes crack development in the shear-critical monolithic beam. No visible cracking was observed up to an actuator displacement of 6 mm (load = 16.7 kips). The first major cracks appeared at 8 mm actuator displacement (load = 25.2 kips). At this displacement, cracking was observed in all regions, including the south shear span. Crack widths at the south region reached approximately 0.25 mm on both front and back faces. Additional cracks were observed in the mid and north regions, with crack widths up to 0.25 mm. The residual crack patterns for the tested shear-critical beams are shown in Figure 42.

Table 9. Crack development in shear-critical monolithic beam

Actuator Displacement (mm)	Load (kips)	No. of Cracks	Max Crack Width (mm)
2	4.1	0	0
4	9.2	0	0
6	16.7	0	0
8	25.2	6	0.3

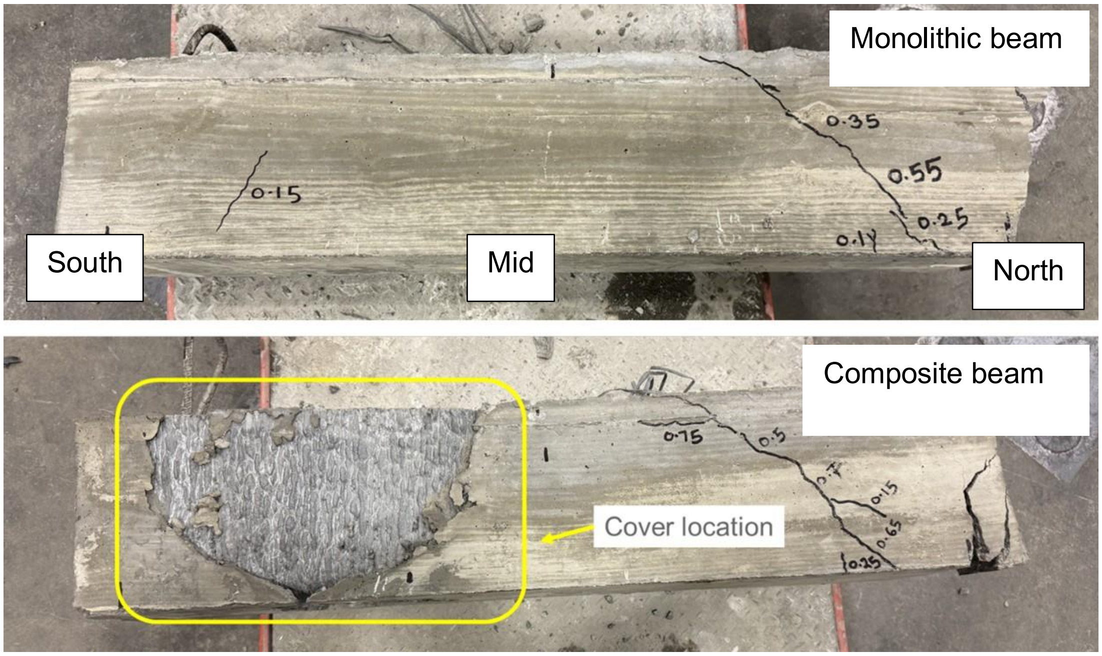

Figure 42. Post-testing residual crack pattern in flexure-critical beams

- Table 10 presents crack development in the shear-critical composite beam with SHCC cover placed at the south shear span. No visible cracking was observed up to an actuator displacement of 6 mm (load = 17.9 kips). At 8 mm actuator displacement (26.5 kip), cracking was observed only outside the SHCC-covered south shear span. Cracks developed in the mid and north regions, with crack widths ranging from 0.20 to 0.25 mm. Importantly, no cracks were recorded in the SHCC-covered south shear span on either face of the beam.

Table 10. Crack development in shear-critical composite beam

Actuator Displacement (mm)	**Load (kips)**	**No. of Cracks***	**Max Crack Width (mm)***
2	3.9	0	0
4	10	0	0
6	17.9	0	0
8	26.5	4	0.3

*Cracks reported occurred outside the SHCC-covered south shear span

- The modifications to the 3D printer implemented in Task 2.9 significantly improved the functionality and reliability of the small-scale printer used in this research. The optimized system provided controlled extrusion, consistent filament geometry, and sufficient buildability for producing SHCC covers with the required dimensional accuracy and surface quality. These enhancements enabled repeatable fabrication of SHCC shells and supported the successful execution of subsequent material and structural testing.

6. Conclusions and recommendations

Conclusions

This study demonstrates the feasibility and effectiveness of using 3D-printed strain-hardening cementitious composite (SHCC) covers as permanent formwork to mitigate cracking in prestressed concrete elements. Through an integrated framework combining numerical modeling, material development, additive manufacturing, and structural testing, the research establishes a clear link between anchorage-zone strain demand and performance-targeted material design. Key conclusions are summarized as follows:

1. Material development - The developed 3D-printable SHCC met the targeted fresh-state rheological requirements and hardened-state mechanical properties, enabling stable extrusion while achieving the tensile strain capacity required for effective crack control.

2. Interlayer bond behavior and improvement - Baseline interlayer bond strength of 3D-printed SHCC was significantly lower than mold-cast tensile capacity, confirming printing-induced anisotropy as a governing limitation for structural performance. Reducing nozzle offset distance and introducing grooved nozzle geometry substantially improved interlayer bond strength, with grooved configurations achieving bond capacities exceeding the tensile strength of printed SHCC.

3. Concrete-SHCC interface bonding and modifications - Axial bond strength between SHCC and conventional concrete exceeded numerical demand, while shear bond strength governed interface performance and required surface modification to enhance composite action. Printing-induced grooves significantly improved shear bond strength at the concrete–SHCC interface, whereas sandblasting did not provide additional benefit and reduced interface performance.

4. Numerical modeling for bonding behavior - Numerical analysis showed that shear demand governs concrete–SHCC bond design, providing a benchmark for evaluating experimental bond adequacy.

5. Proof-of-Concept beam testing - SHCC covers effectively suppressed flexural cracking in the regions where they were applied. Post-test inspections confirmed no delamination between SHCC covers and conventional concrete, validating reliable composite action under mechanical loading.

6. Durability performance - Accelerated corrosion testing showed that SHCC covers limited crack connectivity and reduced corrosion damage compared to conventional concrete specimens.

7. Overall feasibility - The combined experimental and numerical results confirm that 3D-printed SHCC covers provide a feasible, material-efficient solution for mitigating cracking and enhancing durability in prestressed concrete systems.

Recommendations

Based on the findings of this study, the following recommendations are proposed to advance the technology toward practical deployment:

1. Optimization of interface shear resistance - Future work should focus on standardized surface-texturing strategies, such as controlled filament geometry or engineered groove patterns, to ensure consistently high shear bond capacity across different printing systems.

2. Scaling to full-scale girder applications - While laboratory-scale beams demonstrated feasibility, full-scale prestressed girder testing is recommended to evaluate constructability, load transfer, and cracking behavior under realistic prestress release conditions.

3. Printer and nozzle standardization - Development of application-specific nozzle geometries and extrusion controls will improve interlayer bonding, dimensional consistency, and print reliability, especially for complex shell geometries.

4. Long-term durability validation - Extended exposure studies incorporating freeze–thaw cycles, sustained loading, and environmental aging are recommended to quantify long-term performance benefits under field-relevant conditions.

5. Design guidance development - The results of this study can be used to develop preliminary design recommendations linking required SHCC tensile strain capacity, cover thickness, and placement length to anchorage-zone strain demand.

7. Practical application/impact on transportation infrastructure

The findings of this study demonstrate that 3D-printed strain-hardening cementitious composite (SHCC) covers can be practically implemented as permanent formwork to mitigate cracking and improve durability in prestressed concrete bridge girders. The proposed approach aligns well with current precast construction practices and offers a scalable pathway for enhancing the long-term performance of transportation infrastructure without requiring fundamental changes to existing design or fabrication workflows.

Integration into precast bridge girder construction

The SHCC cover system is well-suited for integration into conventional precast prestressed girder manufacturing. The covers can be fabricated using extrusion-based 3D printing, either off-site or directly at precast facilities, and placed into standard steel or modular formwork prior to concrete casting. Because the SHCC shell functions as permanent formwork, it eliminates the need for additional installation steps after casting and does not interfere with prestressing strand placement, reinforcement detailing, or concrete consolidation.

The U-shaped shell geometry allows conventional concrete to be placed and vibrated without obstruction, ensuring compatibility with existing production practices. Prestress transfer, curing, demolding, and handling procedures remain unchanged, minimizing disruption to established fabrication workflows. This compatibility is critical for adoption by precast plants, where production efficiency and repeatability are essential.

Targeted use of advanced concrete materials

A key advantage of the proposed system is its material efficiency. Instead of replacing the entire girder or end region with advanced concrete materials such as UHPC or SHCC, the approach strategically applies SHCC only where it is structurally and durability-critical-namely, in the flexural and anchorage-zone cracking regions. This targeted deployment significantly reduces material costs while still leveraging the high tensile strain capacity and crack-control benefits of SHCC.

By limiting the use of advanced materials to thin cover shells, the system offers a cost-effective alternative to full-section replacement strategies and avoids challenges associated with large-scale use of non-standard materials.

Durability and service life enhancement

Cracking at girder ends and in flexural regions is a primary driver of durability deterioration in prestressed concrete bridges, as cracks provide direct pathways for moisture and chloride ingress. The SHCC cover system addresses this challenge by suppressing crack initiation and limiting crack widths, thereby reducing connectivity between surface cracks and embedded reinforcement.

Experimental results from this study showed negligible cracking within SHCC-protected regions and improved corrosion performance under accelerated exposure conditions. These findings suggest that the use of SHCC covers can significantly slow reinforcement corrosion, reduce maintenance frequency, and extend the service life of bridge girders. Improved durability directly translates to lower life-cycle costs and enhanced reliability of transportation infrastructure.

Structural performance and damage redistribution

The proof-of-concept beam tests demonstrated that SHCC covers do not compromise structural capacity. Instead, the presence of the cover altered the governing failure mechanism by shifting damage away from the protected flexural zone to unprotected regions. This redistribution of damage is beneficial from a design and maintenance perspective, as it protects critical regions most susceptible to durability-related deterioration.

The ability of the SHCC cover to maintain composite action without delamination further supports its use in structural applications where reliable load transfer and long-term performance are essential.

Scalability and technology readiness

The use of extrusion-based 3D printing makes the SHCC cover system inherently scalable. Printing parameters, nozzle geometries, and shell dimensions can be adjusted to accommodate different girder sizes, shapes, and design requirements. As commercial construction-scale concrete printers become more widely available, the fabrication of SHCC covers can be automated and standardized, further improving production efficiency and quality control.

The results of this study position the SHCC cover system at an early but promising stage of technology readiness, suitable for pilot-scale demonstrations and full-scale validation testing in collaboration with DOTs and precast manufacturers.

Potential broader applications

While this study focused on prestressed bridge girders, the concept of 3D-printed SHCC permanent formwork can be extended to other transportation infrastructure components, including reinforced concrete beams, pier caps, deck overhangs, and precast panels, where crack control and durability are critical. This adaptability further enhances the long-term impact of the proposed approach.

8. References

[1] P. Okumus, R. P. Kristam, and M. Diaz Arancibia, "Sources of Crack Growth in Pretensioned Concrete-Bridge Girder Anchorage Zones after Detensioning," *Journal of Bridge Engineering,* vol. 21, no. 10, 2016, doi: 10.1061/(asce)be.1943-5592.0000928.

[2] P. Okumus and M. G. Oliva, "Evaluation of crack control methods for end zone cracking in prestressed concrete bridge girders," *PCI Journal,* vol. 58, no. 2, pp. 91-105, 2013, doi: 10.15554/pcij.03012013.91.105.

[3] P. Okumus, M. G. Oliva, and S. Becker, "Nonlinear finite element modeling of cracking at ends of pretensioned bridge girders," *Engineering Structures,* vol. 40, pp. 267-275, 2012/07/01/ 2012, doi: https://doi.org/10.1016/j.engstruct.2012.02.033.

[4] C. Y. Tuan, S. A. Yehia, N. Jongpitaksseel, and M. K. Tadros, "End Zone Reinforcement for Pretensioned Concrete Girders," *PCI Journal,* vol. 49, no. 3, pp. 68-82, 2004, doi: 10.15554/pcij.05012004.68.82.

[5] B. E. Ross, H. R. Hamilton, and G. R. Consolazio, "Experimental and Analytical Evaluations of Confinement Reinforcement in Pretensioned Concrete Beams," *Transportation Research Record: Journal of the Transportation Research Board,* vol. 2251, no. 1, pp. 59-67, 2011, doi: 10.3141/2251-06.

[6] W. T. Marshall and A. H. Mattock, "Control of Horizontal Cracking in the Ends of Pretensioned Prestressed Concrete Girders," *PCI Journal,* vol. 7, no. 5, pp. 56-74, 1962, doi: 10.15554/pcij.10011962.56.74.

[7] J. Kannel, C. French, and H. Stolarski, "Release Methodology of Strands to Reduce End Cracking in Pretensioned Concrete Girders," *PCI Journal,* vol. 42, no. 1, pp. 42-54, 1997, doi: 10.15554/pcij.01011997.42.54.

[8] P. Gergely and M. A. Sozen, "Design of Anchorage-Zone Reinforcement in Prestressed Concrete Beams," *PCI Journal,* vol. 12, no. 2, pp. 63-75, 1967, doi: 10.15554/pcij.04011967.63.75.

[9] V. S. Ronanki, S. Aaleti, and J. P. Binard, "Long-Span Hybrid Precast Concrete Bridge Girder Using Ultra-High-Performance Concrete and Normalweight Concrete," *PCI Journal,* vol. 64, no. 6, 2019, doi: 10.15554/pcij64.6-02.

[10] H. Li, L. Li, X. Fan, M. Ye, X. Shao, and L. Yi, "Experimental and numerical investigation on the flexural behavior of a large-scale prestressed UHPC T-Shaped girder," *Engineering Structures,* vol. 272, 2022, doi: 10.1016/j.engstruct.2022.115027.

[11] K. Ragalwar, W. F. Heard, B. A. Williams, and R. Ranade, "Significance of the particle size distribution modulus for strain-hardening-ultra-high performance concrete (SH-UHPC) matrix design," *Construction and Building Materials,* vol. 234, 2020, doi: 10.1016/j.conbuildmat.2019.117423.

[12] V. C. Li, *Engineered Cementitious Composites (ECC)*. 2019.

[13] H. Ma, C. Yi, and C. Wu, "Review and outlook on durability of engineered cementitious composite (ECC)," *Construction and Building Materials,* vol. 287, 2021, doi: 10.1016/j.conbuildmat.2021.122719.

[14] H. Liu, Q. Zhang, V. Li, H. Su, and C. Gu, "Durability study on engineered cementitious composites (ECC) under sulfate and chloride environment," *Construction and Building Materials,* vol. 133, pp. 171-181, 2017, doi: 10.1016/j.conbuildmat.2016.12.074.

[15] E. Ivaniuk *et al.*, "Application-Driven Material Design of Printable Strain Hardening Cementitious Composites (SHCC)," *Materials,* vol. 15, no. 5, 2022, doi: 10.3390/ma15051631.

[16] L. Li, Z. Cai, K. Yu, Y. X. Zhang, and Y. Ding, "Performance-based design of all-grade strain hardening cementitious composites with compressive strengths from 40 MPa to 120 MPa," *Cement and Concrete Composites,* vol. 97, pp. 202-217, 2019, doi: 10.1016/j.cemconcomp.2019.01.001.

[17] V. C. Li *et al.*, "On the emergence of 3D printable Engineered, Strain Hardening Cementitious Composites (ECC/SHCC)," *Cement and Concrete Research,* vol. 132, 2020, doi: 10.1016/j.cemconres.2020.106038.

[18] E. Ivaniuk, M. Friedrich Eichenauer, Z. Tošić, S. Müller, D. Lordick, and V. Mechtcherine, "3D printing and assembling of frame modules using printable strain-hardening cement-based composites (SHCC)," *Materials & Design,* vol. 219, 2022, doi: 10.1016/j.matdes.2022.110757.

[19] N. Xu and Y. Qian, "Effects of fiber volume fraction, fiber length, water-binder ratio, and nanoclay addition on the 3D printability of strain-hardening cementitious composites (SHCC)," *Cement and Concrete Composites,* vol. 139, 2023, doi: 10.1016/j.cemconcomp.2023.105066.

[20] A. L. van Overmeir, B. Šavija, F. P. Bos, and E. Schlangen, "3D printable strain hardening cementitious composites (3DP-SHCC), tailoring fresh and hardened state properties," *Construction and Building Materials,* vol. 403, 2023, doi: 10.1016/j.conbuildmat.2023.132924.

[21] Y. Sun, G. Du, X. Deng, and Y. Qian, "Effects of nozzle thickness on the mechanical properties of 3D printable Ultra-High Performance Strain-Hardening Cementitious Composites (UHP-SHCC)," *Construction and Building Materials,* vol. 489, 2025, doi: 10.1016/j.conbuildmat.2025.142128.

[22] N. Xu, Y. Qian, J. Yu, and C. K. Y. Leung, "Tensile performance of 3D-printed Strain-Hardening Cementitious Composites (SHCC) considering material parameters, nozzle

size and printing pattern," *Cement and Concrete Composites,* vol. 132, 2022, doi: 10.1016/j.cemconcomp.2022.104601.

[23] J. Yu and C. K. Y. Leung, "Impact of 3D Printing Direction on Mechanical Performance of Strain-Hardening Cementitious Composite (SHCC)," in *First RILEM International Conference on Concrete and Digital Fabrication – Digital Concrete 2018*, (RILEM Bookseries, 2019, ch. Chapter 24, pp. 255-265.

[24] K. Nefs, K. C. J. de Kroon, J. Sloots, F. P. Bos, and T. A. M. Salet, "Orientation Dependency of 3D printed SHCC at increasing length scale," *Cement and Concrete Composites,* vol. 149, 2024, doi: 10.1016/j.cemconcomp.2024.105515.

[25] J. Guan, L. Wang, Q. Wan, and G. Ma, "Material and structural fatigue performance of 18 m-span reinforced arch structure manufactured by 3D printing concrete as permanent formwork," *Engineering Structures,* vol. 328, 2025, doi: 10.1016/j.engstruct.2025.119734.

[26] B. Liu *et al.*, "Study on the compression performance of 3D printing concrete permanent formwork composite columns," *Journal of Building Engineering,* vol. 98, 2024, doi: 10.1016/j.jobe.2024.111245.

[27] J. Guan, L. Wang, Y. Huang, G. Ma, and Y. Tao, "Evaluation of the Performance of Reinforced Concrete Beams with 3D-Printed Permanent Formwork," *Journal of Intelligent Construction,* vol. 2, no. 4, pp. 1-17, 2024, doi: 10.26599/jic.2024.9180030.

[28] L. Wang, Y. Yang, L. Yao, and G. Ma, "Interfacial bonding properties of 3D printed permanent formwork with the post-casted concrete," *Cement and Concrete Composites,* vol. 128, 2022, doi: 10.1016/j.cemconcomp.2022.104457.

[29] H. Fakhri, K. A. Ragalwar, and R. Ranade, "On the use of Strain-Hardening Cementitious Composite covers to mitigate corrosion in reinforced concrete structures," *Construction and Building Materials,* vol. 224, pp. 850-862, 2019, doi: 10.1016/j.conbuildmat.2019.07.052.

[30] M. Smith, *ABAQUS/Standard User's Manual, Version 6.9*. Dassault Syst{\`e}mes Simulia Corp (in English), 2009.

[31] M. R. O'Callaghan and O. Bayrak, *Tensile stresses in the end regions of pretensioned i-beams at release*. The University Of Texas At Austin, 2008.

[32] *ASTM C1437, Standard test method for flow of hydraulic cement mortar*. 2020.

[33] D. G. Soltan and V. C. Li, "A self-reinforced cementitious composite for building-scale 3D printing," *Cement and Concrete Composites,* vol. 90, pp. 1-13, 2018, doi: 10.1016/j.cemconcomp.2018.03.017.

[34] *ASTM C143, Standard Test Method for Slump of Hydraulic-Cement Concrete*. ASTM International, West Conshohocken, PA, 2016, 2020.

[35] *ASTM C109, Standard Test Method for Compressive Strength of Hydraulic Cement Mortars (Using 2-in. or [50-mm] Cube Specimens)*. 2024.

[36] D. Kumar and R. Ranade, "Influence of matrix-modification and fiber-hybridization on high-temperature residual mechanical performance of strain-hardening cementitious composites," *Construction and Building Materials,* vol. 302, 2021, doi: 10.1016/j.conbuildmat.2021.124157.

[37] *ASTM C78, Standard Test Method for Flexural Strength of Concrete (Using Simple Beam with Third-Point Loading)*. 2022.

[38] *ASTM G1-25, Standard Practice for Preparing, Cleaning, and Evaluating Corrosion Test Specimens*. ASTM International, West Conshohocken, PA, 2025, 2025.

[39] *Building Code Requirements for Structural Concrete and Commentary (Reapproved 2022): ACI CODE-318-19(22)*. Farmington Hills, MI : American Concrete Institute, 2019.

[40] *ASTM C595-08a, Standard Specification for Blended Hydraulic Cements*. ASTM International, West Conshohocken, PA, 2016, 2025.

[41] *ASTM C192, Standard Practice for Making and Curing Concrete Test Specimens in the Laboratory*. ASTM International, West Conshohocken, PA, 2016, 2025.

[42] *ASTM C618, Standard Specification for Coal Ash and Raw or Calcined Natural Pozzolan for Use in Concrete*. ASTM International, West Conshohocken, PA, 2016, 2025.

[43] *ASTM C494, Standard Specification for Chemical Admixtures for Concrete*. ASTM International, West Conshohocken, PA, 2016, 2025.

[44] *ASTM A615, Standard Specification for Deformed and Plain Carbon-Steel Bars for Concrete Reinforcement*. ASTM International, West Conshohocken, PA, 2016, 2024.

9. Acknowledgements

This work is supported by the US Department of Transportation, Tier 1 University Transportation Center (Transportation Infrastructure Precast Innovation Center) and Institute of Bridge Engineering, University at Buffalo, The State University of New York. Any opinions, findings, conclusions, or recommendations expressed in this material are those of the authors and do not necessarily reflect the views of the supporting agencies.